Robotics and Computer–Integrated Manufacturing 84 (2023) 102581

Contents lists available at ScienceDirect

Robotics and Computer-Integrated Manufacturing

journal homepage: www.elsevier.com/locate/rcim

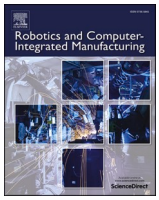

# Multisensor fusion-based digital twin for localized quality prediction in robotic laser-directed energy deposition

Lequn Chen [a,b], Guijun Bi [c], Xiling Yao [d,*], Chaolin Tan [a], Jinlong Su [a], Nicholas Poh Huat Ng [b], Youxiang Chew [a], Kui Liu [d], Seung Ki Moon [b,*]

[a] Advanced Remanufacturing and Technology Centre (ARTC), A*STAR, 3 Cleantech Loop, 637143, Singapore
[b] School of Mechanical and Aerospace Engineering, Nanyang Technological University, 639798, Singapore
[c] Institute of Intelligent Manufacturing, Guangdong Academy of Sciences, Guangzhou, 510070, China
[d] Singapore Institute of Manufacturing Technology (SIMTech), A*STAR, 5 Cleantech Loop, 636732, Singapore

ARTICLE INFO

*Keywords:*
Additive Manufacturing
In-situ defect detection
Laser-directed energy deposition
Machine learning
Multisensor fusion

ABSTRACT

Early detection of defects, such as keyhole pores and cracks is crucial in laser-directed energy deposition (L-DED) additive manufacturing (AM) to prevent build failures. However, the complex melt pool behaviour cannot be adequately captured by conventional single-modal process monitoring approaches. This study introduces a multisensor fusion-based digital twin (MFDT) for localized quality prediction in the robotic L-DED process. The data used in multisensor fusion includes features extracted from a coaxial melt pool vision camera, a microphone, and an off-axis short wavelength infrared thermal camera. The key novelty of this work is a spatiotemporal data fusion method that synchronizes multisensor features with the real-time robot motion data to achieve localized quality prediction. Optical microscope (OM) images of the printed part are used to locate defect-free and defective regions (i.e., cracks and keyhole pores), which serve as ground truth labels for training supervised machine learning (ML) models for quality prediction. The trained ML model is then used to generate a virtual quality map that registers quality prediction outcomes within the 3D volume of the printed part, thus eliminating the need of physical inspections by destructive methods. Experiments show that the virtual quality map closely matches the actual quality observed by OM. Compared to traditional single-sensor-based quality prediction, the MFDT has achieved a significantly higher quality prediction accuracy (96%), a higher ROC-AUC score (99%), and a lower false alarm rate (4.4%). As a result, the MFDT is a more reliable method for defect prediction. The proposed MFDT also lays the groundwork for our future development of a self-adaptive hybrid processing strategy that combines machining with AM for defect removal and quality improvement.

## 1. Introduction

Additive manufacturing (AM) has shown remarkable potential in manufacturing geometrically complex products with improved mechanical performance, reduced weight, and shortened product design and development lifecycles [1–3]. In particular, laser-directed energy deposition (L-DED) process has been applied for the manufacturing of large-scale metallic parts in the aerospace, marine, and offshore industries [4–8]. However, maintaining high quality consistency, dimensional accuracy, and process repeatability remains a substantial challenge in such large-format metal AM techniques. Despite employing pre-optimized process parameters, defects such as cracks and keyhole pores might still occur due to localized heat accumulation, surface fluctuation, speed inconsistencies, and gas entrapment [9–11]. Pores and cracks formed during the AM process can severely impair the mechanical performance of the printed parts. Therefore, early detection and correction of defects are crucial in AM to prevent build failures.

Recently, significant efforts have been made for in-situ monitoring and defect detection in AM [12–16]. The state-of-the-art in-process sensing technologies utilize either vision or infrared (IR) thermal sensors to capture the process characteristics (e.g., melt pool geometries, acoustic emissions, temperature histories, etc.), combined with machine learning (ML) models for defect prediction. One of the most widely used methods in various AM processes is vision-based in-situ monitoring [17–19]. For example, real-time surface defect detection can be achieved by a vision camera with deep learning-based object detection

* Corresponding authors.
*E-mail addresses:* yaox@outlook.com (X. Yao), skmoon@ntu.edu.sg (S.K. Moon).

https://doi.org/10.1016/j.rcim.2023.102581
Received 20 January 2023; Received in revised form 18 March 2023; Accepted 2 May 2023
Available online 20 May 2023

algorithms, which was successfully implemented in wire and arc additive manufacturing (WAAM) [20,21] and AM-fabricated continuous fibre-reinforced polymer [22]. For laser-based AM processes, a vision sensor with near-infrared (NIR) optical filters can be applied to monitor molten pool dynamic behaviours [9], which can be used for deposition height detection [23], closed-loop feedback control [24–26], and distinguishing melting states through melt pool motion features [27]. Furthermore, with additional temperature information, an IR thermal camera can be more effective than a visual sensor for observing in-situ melt pool dynamics. For instance, Criales et al. [28] used in-situ thermal camera recording to investigate the effects of process parameters and scan strategies on the melt pool size and shape, as well as powder particle spattering and heating and cooling rates during laser powder bed fusion (L-PBF). It was discovered that dynamic fluctuations in melt pool geometries were linked to microstructure characteristics. Grasso et al. [29] also extracted essential temperature features and conducted statistical analysis to detect unstable behaviour of the process plume during the L-PBF. Khanzadeha et al. [30] developed a real-time porosity prediction method using melt pool morphological features extracted from thermal images. Supervised ML approaches were used to classify melt pools to predict porosity within the parts. Similarly, Mao et al. utilized thermal signatures and a Convolutional neural network (CNN) for lack of fusion (LoF) porosity prediction [31]. Other porosity prediction methods using optical thermal imaging were also reported in [32–34].

Apart from vision and infrared thermal sensing approaches, acoustic monitoring has recently emerged as a more versatile and cost-effective alternative for in-situ defect detection in AM. Compared to vision and thermal sensors, acoustic sensors require minimal modifications to AM machines and have a significantly higher sensitivity to laser-material interactions [35]. Shevchik et al. [36,37] used a fibre Brag grating (FBG) sensor to capture acoustic emission (AE) signals related to LoF porosity defects in the L-PBF process. The deep CNN model was trained on wavelet transform (WT) characteristics to predict porosities and achieved 89% accuracy. Subsequently, Drissi-Daodi et al. [38] proposed a CNN-based AE signal classification approach to differentiate process regions, including conduction mode, keyhole porosity, LoF porosity, and balling defects in different materials. Instead of the FBG sensor, they employed a low-cost microphone sensor to capture airborne AE signals. Tempelman et al. [24] used acoustic monitoring to detect keyhole pores formation in L-PBF. A support vector machine (SVM) classifier was trained on spectral features to identify keyhole pores formation with up to 97% accuracy within 7.5 ms. Bevans et al. [24] introduced in-situ acoustic sensing to identify flaw formation in the metal inert gas electric arc welding process. To detect flaws, a wavelet graph signal analysis was applied to extract features from the arc sound. However, acoustic monitoring in L-DED is significantly more challenging than in L-PBF and WAAM processes due to the noisy surroundings. Recently, an acoustic denoising strategy for L-DED was proposed in [39], and a CNN model trained on Mel-Frequency Cepstral Coefficients (MFCCs) was used to classify the laser-material interaction sound in L-DED in order to predict cracks and keyhole pore formations [40].

The aforementioned in-situ monitoring methods have shown potential in predicting specific types of defects (e.g., LoF, balling, keyhole pores, etc.) for online monitoring of the AM process. Nevertheless, there are two major limitations in the existing methods: (1) the lack of location-specific quality prediction capability and (2) the lack of robust and reliable defect prediction models for real production as opposed to specimen creation with artificially introduced defects. ML models for in-situ defect prediction in most existing methods are trained by data acquired from purposefully created defective components with suboptimal process settings. However, in a real production context, the product is manufactured using pre-optimized process parameters, and defects may stochastically occur in different locations throughout the part volume. Furthermore, the traditional single-modal sensing technique is unable to capture the complex melt pool behaviour. Vision sensors can only provide geometric information about the melt pool. The vision camera's restricted temperature sensitivity range might not be sufficient for process monitoring [41]. Thermal sensors in the short wavelength infrared (SWIR) band typically necessitate a time-consuming temperature calibration procedure. The emissivity of heat affected zone is governed by a number of factors, including material phase, temperature, and surface roughness. Inaccuracies in temperature measurements can jeopardize the robustness of defect prediction. Although the acoustic sensing approach has high sensitivity, it is susceptible to environment noises. As a result, no single sensing approach could predict defects and part quality in a holistic and robust manner. To address this challenge, multisensor monitoring has been proposed as it is able to alleviate the disadvantages of individual sensors and allow for a more robust and reliable defect prediction [42].

Prior research has been reported on multisensor monitoring and data fusion for laser-based AM. Pandiyan et al. [43] proposed a deep learning-assisted multimodal sensing strategy that integrates four sensors (back reflection (BR), Visible, Infrared (IR), and AE) to predict defective regions in the L-PBF process. The authors demonstrated that the BR and AE sensors could be more informative than the vision and IR sensors. In addition, a feature-level fusion method was proposed by Li et al. [44,45] for L-PBF, where in-situ signal features from a photodiode and a microphone were fused using a CNN-based model to predict quality. The fusion of two sensor information outperformed the single-modal prediction. Perani et al. [46] applied a CNN-based architecture to predict track geometry deposited by L-DED by fusing coaxial melt pool images with process input data (e.g., laser power and speed command, laser activation status (ON/OFF)). As compared to traditional single-modal online-monitoring approaches, the proposed method can predict localized track size with high accuracy. Petrich et al. [47] also conducted a proof-of-concept study on multimodal sensor fusion in L-PBF, and reported that incorporating additional information from other sensing modalities can considerably improve single optical imaging-based defect prediction. However, multisensor fusion in the L-DED for internal quality mapping was rarely reported due the lack of spatiotemporal fusion attempts that could generate data features useful for localized defect prediction.

In this paper, a multisensor fusion-based digital twin (MFDT) is proposed for location-specific quality prediction in the robotic L-DED process. The key novelty of this work is a spatiotemporal data fusion method that synchronizes multisensor features with the real-time robot motion data to achieve localized quality prediction. In this research, three sensors are used during the data fusion: (1) a coaxial vision camera for melt pool geometry monitoring, (2) a microphone sensor capturing the laser-material interaction sound, and (3) an off-axis SWIR thermal camera monitoring the temperature field. Real-time robot tool-centre-point (TCP) positions are acquired from the robot controller. Ex-situ optical microscope (OM) images of printed parts are used to locate defect-free and defective regions (i.e., cracks and keyhole pores), which serve as ground truth labels for training supervised machine learning (ML) models for localized quality prediction. The trained ML model is then used to generate a virtual quality map that registers quality prediction outcomes within the 3D volume of the printed part, thus eliminating the need of physical inspections by destructive methods. Experimental results demonstrate that the virtual quality map closely matches the actual quality observed by OM. In addition, compared to traditional single-sensor-based quality prediction methods, the MFDT has achieved a significantly higher defect prediction accuracy (96%), a higher ROC-AUC score (99%), and a lower false alarm rate (4.4%). Therefore, the proposed MFDT is proven to be a reliable and robust approach for defect prediction. The proposed MFDT also sets the foundations for our future development of a self-adaptive hybrid processing strategy that combines machining with AM for defect removal and quality improvement.

The rest of the paper is organized as follows. Section 2 introduces the overall framework of the proposed MFDT. Section 3 describes the

experimental procedures, software architecture, as well as the subsystems and data processing methods in the MFDT that leads to the localized quality prediction and mapping capability. Section 4 presents the results of the MFDT evaluation and validation with comparisons between MFDT and traditional single-sensor-based defect prediction methods. Finally, Section 5 concludes the study by summarizing the key findings and proposing future work on MFDT for a self-adaptive hybrid processing strategy.

## 2. Overview of the framework

Fig. 1 depicts an overview of the proposed multisensor fusion-based digital twin (MFDT) framework for localized defect prediction. The proposed MFDT consists of four main steps:

i A multisensor in-situ monitoring setup with Robot Operating System (ROS)-based software platform is developed. Sensor-captured process data includes coaxial melt pool images, temperature field data, and acoustic signals during the robotic L-DED process. Sections 3.1 and 3.2 show the system configuration and software architectures, respectively.

ii Key features are extracted from each sensor, and spatiotemporal data fusion is performed to synchronize and register the multisensor features within the part's 3D volume. It is the prerequisite for subsequent quality prediction. Details on the feature extractions and data fusion method are described in Sections 3.3-3.5.

iii After multisensor feature extraction and selection, various supervised machine learning (ML) models are trained to map the spatiotemporally fused datasets to the quality labels within the entire volumetric domain. Ex-situ quality inspections via optical microscopy (OM) are conducted to locate defect-free regions as well as keyhole pores and cracks. The output class of the ML models had four labels: 'laser-off', 'defect-free', 'cracks' and 'keyhole pores'. Cracks and keyhole pores are considered as defective regions that must be removed once they are detected to avoid further quality deterioration. Among the tested ML classifiers, neural networks (NN) outperformed all others and are deployed on the ROS-based software platform.

iv The trained ML model is used to identify regions to be removed during the L-DED process. A virtual quality map that registered quality prediction outcomes within the 3D volume of the printed part is generated. Defect boundaries can be extracted from the virtual quality map for subsequent defect correction using robotic machining.

The following section describes the details of the system setup, software architectures, experimental procedures, and individual components and data processing steps in the MFDT.

## 3. Methodology

### 3.1. System setup and experimental procedures

Fig. 2(a) depicts a dual-robot hybrid additive-subtractive manufacturing system. The system consisted of a robotic L-DED cell and a robotic machining cell. In the L-DED process, a 6-axis industrial robot carried a coaxial powder-blown nozzle, while a 2-axis positioner held the workpiece [48]. A 1070 nm laser beam melted the powder material as it was injected into the substrate, forming a melt pool. As the nozzle travelled in the feed direction, the molten material solidified rapidly in the molten pool area. For the robotic machining process, the milling spindle was mounted on the end-effector of the industrial robot.

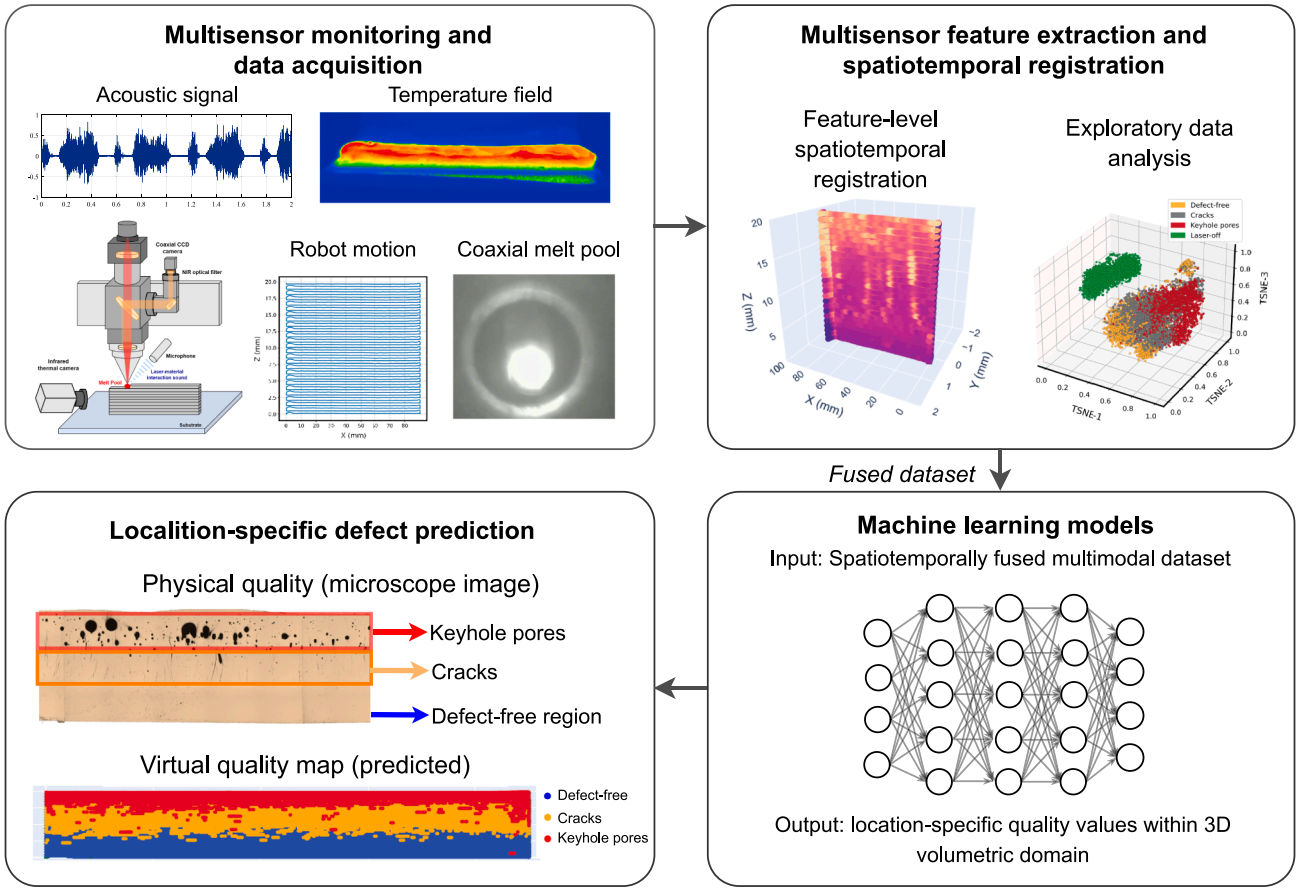


**Fig. 1.** The proposed multisensor fusion-based digital twin (MFDT) framework for location-dependent defect prediction in robotic L-DED.

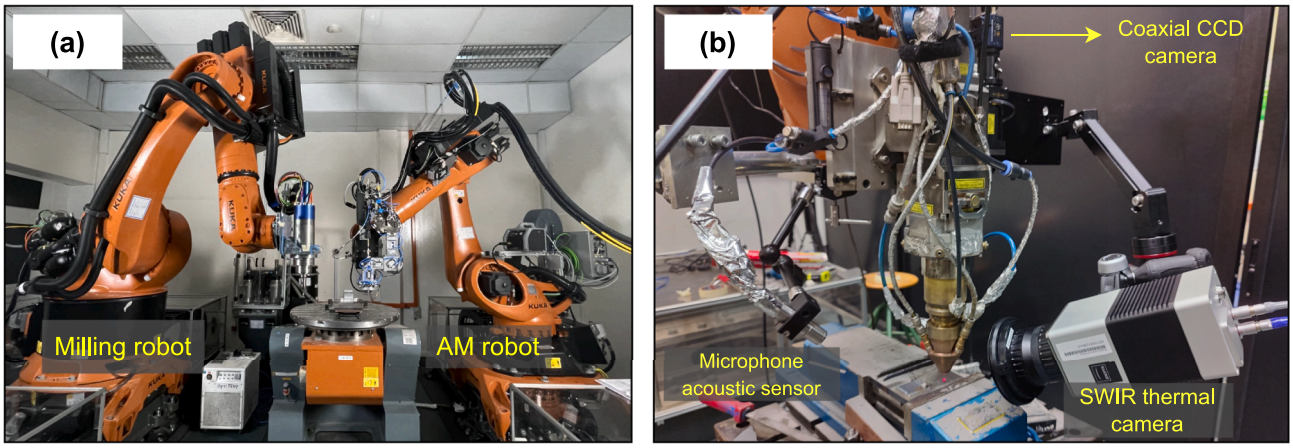


**Fig. 2.** Experimental setup. (a) Dual-robot hybrid additive-subtractive manufacturing system from SIMTech; (b) multisensor monitoring setup for robotic L-DED.

When the MFDT detected flaws during the L-DED process, the AM process can be stopped, and robotic machining was used to remove the defective regions. The dual-robot hybrid system with a high degree of freedom (DoF) enables flexible fabrication of extremely large workpieces and paves the path for self-adaptive hybrid processing.

As shown in Fig. 2(b) and Fig. 3, three sensors were integrated into the robotic L-DED for in-situ process monitoring:

- A thermal infrared camera was placed next to the printed part to monitor the temperature field of the printed part's region of interest (ROI) at a frequency of 30 Hz. The thermal image processing technique presented in our earlier work [49] was used to extract key temperature features.
- A coaxial CCD camera with an acquisition frequency of 30 Hz was mounted on the laser head. The coaxial visual melt pool image was acquired by the visible spectrum CCD camera through a set of reflecting lenses. An optical NIR band-pass filter was attached to the camera lens to isolate the melt pool from the surrounding spatters.
- A microphone sensor was used to capture the laser-material interaction sound during the L-DED process. The microphone had a frequency response range of 50 – 20,000 Hz and was positioned near the laser nozzle. The sampling rate was set to 44,100 Hz. The sound

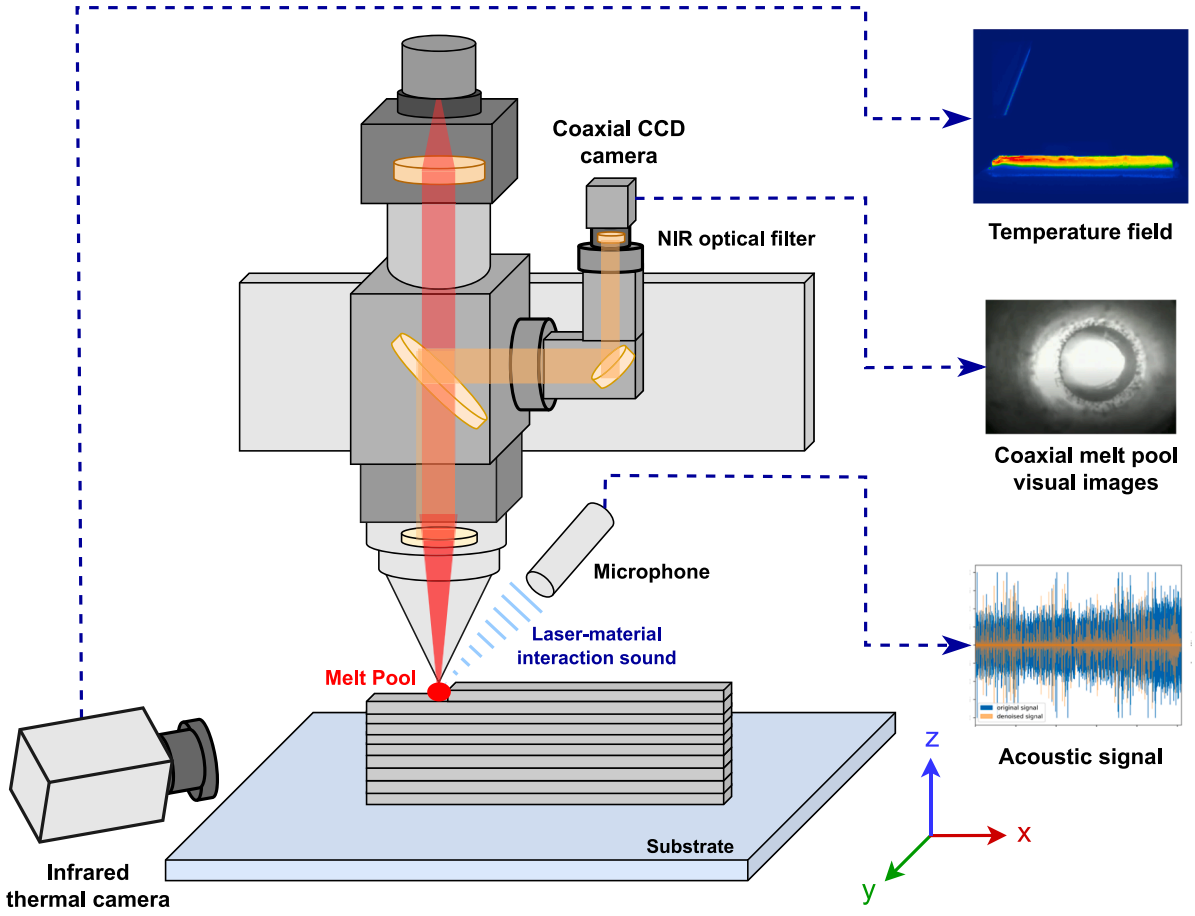


**Fig. 3.** The schematic diagram of the multisensor monitoring for the robotic L-DED system.

contained noise, such as inert gas flow, machine movement and powder flow. Our previous work on acoustic signal denoising [39] was used to extract laser-material interaction sound.

Apart from the sensing modalities mentioned above, a laser displacement sensor was used to detect surface defects and perform in-process adaptive dimension correction, as detailed in our previous work [50–53]. The built-in servo encoders from the KUKA robot measured joint position at a frequency of 250 Hz. Ethernet communication between the robot controller and a personal computer (PC) was used to obtain robot tool-centre-point (TCP) position data. All sensing modalities were connected to the PC running an Ubuntu operating system and an in-house developed software platform with ROS.

In this research, we created a multimodal dataset by producing six single bead wall components with different process parameters and varying dwell time (i.e., 0, 5, 10 seconds) between the layers using commercial maraging steel C300 powder, as shown in Table 1. Unlike most sensor-based defect detection studies in the literature, we did not intentionally manufacture flaws by using suboptimal parameters. Instead, we used pre-optimized process parameters from start to end to deposit materials, enabling us to observe the shift from the defect-free to the defective regime. We kept the energy density (P/v) constant (0.92 kW·s /mm) while increasing the laser power (P) and scanning speed (v) proportionally for the two sets of process parameters (2.3 kW, 25 mm/s and 2.53 kW, 27.5 mm/s). Each process parameter combination was printed once. The dwell length between each layer was increased (from 0 to 5 to 10 seconds) to postpone the onset of defects since it provides cooling time to reduce localized heat build-up. As a result, defects appeared in different locations of the part for different samples. The sample fabricated with a longer dwell period contained fewer flaws. Cracks and keyhole pores emerged at a higher layer in samples fabricated with longer dwell time. Optical microscope (OM) images were collected for each sample to determine the locations of cracks and keyhole pores inside the component. The OM images were used as physical quality labels that served as ground truth for defect prediction. Fig. 4 depicts the sample wire-cutting, ex-situ quality inspections, and location-specific quality registration procedures. The wire-cutting process removes the outer surface of the single bead wall, allowing us to observe the location-specific quality. We took OM image of the x-z surface rather than the y-z cross-sections. This simplifies the data labelling procedure since we can register the multisensor signals along the deposition toolpath with the location of the corresponding defect. Hot cracks and keyhole pores were observed in the OM image as a result of localized heat accumulation. The rapid heating and cooling cycles in single bead wall deposition resulted in unstable melt pools, causing material evaporation and the formation of large gas-entrapped keyhole pores. High thermal stresses on metal caused by a higher concentration rate of solidifying metal can induce hot cracks. Keyhole pores are often large spheroidal shapes with diameters of several millimetres, while hot cracks have lengths of several millimetres, as seen in the Fig. 4.

**Table 1**
L-DED process parameters and setup during the experiments for multisensor data collection.

| Parameters | Values |
|---|---|
| Part geometry | Single bead wall structure |
| Dimension | 90 mm * 42.5 mm |
| Number of layers per sample | 50 |
| Laser power (kW) | [2.3, 2.53] |
| Speed (mm/s) | [25, 27.5] |
| Dwell time between the layers (s) | [0, 5, 10] |
| Laser beam diameter (mm) | 2 |
| Powder flow rate (g/min) | 12 |
| Energy density (kW·s /mm) | 0.92 |
| Hatch space (mm) | 1 |
| Layer thickness (mm) | 0.85 |
| Stand-off distance (mm) | 12 |
| Material | Maraging Steel C300 |
| Types of defects generated | Cracks, keyhole pores |

In this research, we did not seek for individual defects detection. Instead, we conduct region-based defect prediction. i.e., the ML model predicts the "quality regions" to which current time stamp belongs. A "quality region" is defined by a signal segment (500 ms) that corresponds to approximately 12 mm of deposition length. If cracks or keyhole pores occurred within the segment, the entire segment was labelled as "cracks" or "keyhole pores". Despite the fact that the OM image indicated certain gaps between the cracks and pores, such gaps were labelled with the same category as their neighbouring defect. This region-based data annotation is due to two reasons: (1) if the neighbouring region contains cracks or porosity, the overall region quality is poor. Regardless of how many cracks or pores exist, the entire region must be removed; (2) the gaps between the defects are extremely narrow (only around 1-2 mm). Defects are in close proximity to one another. As a result, identifying precise pores or cracks in the signal is extremely challenging. The quality in the neighborhood of a defect is assumed to belong to the same defective category, which avoids mismarking and enhances model robustness to certain multisensor signal. The length of the region (i.e., 500 ms) was chosen as a compromise between ML model accuracy and spatiotemporal resolutions.

The following sub-section will introduce the overall software architecture of the proposed MFDT.

### 3.2. Software architecture

A software platform was developed to implement the proposed MFDT framework. Fig. 5 shows the software architecture, which leveraged on a similar ROS-based multi-nodal architecture as in [54] and [52] to enable PC-sensor/robot communications. The details are explained as follows:

- The raw signal from each sensor is acquired by the sensor SDK driver nodes. The raw acoustic signal, raw thermal images, and raw coaxial melt pool images are published to three separate ROS topics, which are then used for in-situ data processing. The raw acoustic signal is extracted at 44,100 Hz. The raw coaxial vision images and thermal images are extracted at 30 Hz. Meanwhile, a PC-robot interface based on ROS-industrial packages and KUKA Robot Sensor Interface is developed, which extracted the robot's real-time TCP position data at 250 Hz.
- As the raw data from each sensor is retrieved by the driver nodes, subsequent in-situ data processing and feature extraction procedures, such as acoustic signal denoising, temperature feature extraction, and coaxial image processing, are carried out in separate nodes. The key sensor data features, such as acoustic spectrum descriptors, melt pool morphologies (width, length, contour area, etc.), and temperature information, are published to various ROS topics and can be visualized in real-time using the PlotJuggler tool [55]. These extracted features from different sensing modalities are published at a frequency of 30 Hz. Since all the multisensor feature extraction nodes are executed in parallel at the same time stamp, they can be synchronized with the real-time robot position data.
- The trained ML model is implemented in a ROS node, which subscribes to the key multisensor features and predicts various quality categories including laser-off, defect-free, cracks and keyhole pores. The prediction outcomes are made accessible as a ROS topic published at 30 Hz. The predicted quality value is also registered with the robot TCP position data, which provided spatial information about the defect locations.
- Finally, a virtual quality map is generated by subscribing to both TCP position data and the predicted quality outcomes. The virtual quality map can show the predicted quality values within the 3D volume of the deposited part, thus eliminating the need of physical inspections by destructive methods. Furthermore, the milling head can be moved

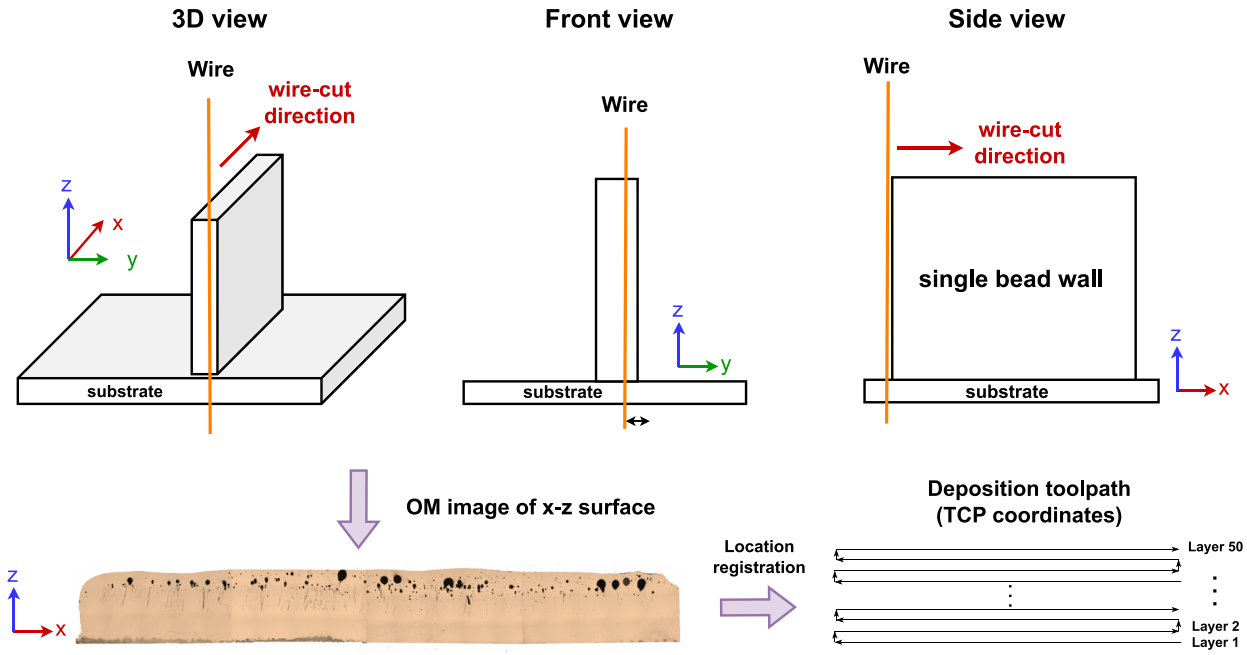


**Fig. 4.** Sample wire-cutting schematic, ex-situ quality inspections utilizing OM images, and location-specific quality registrations.

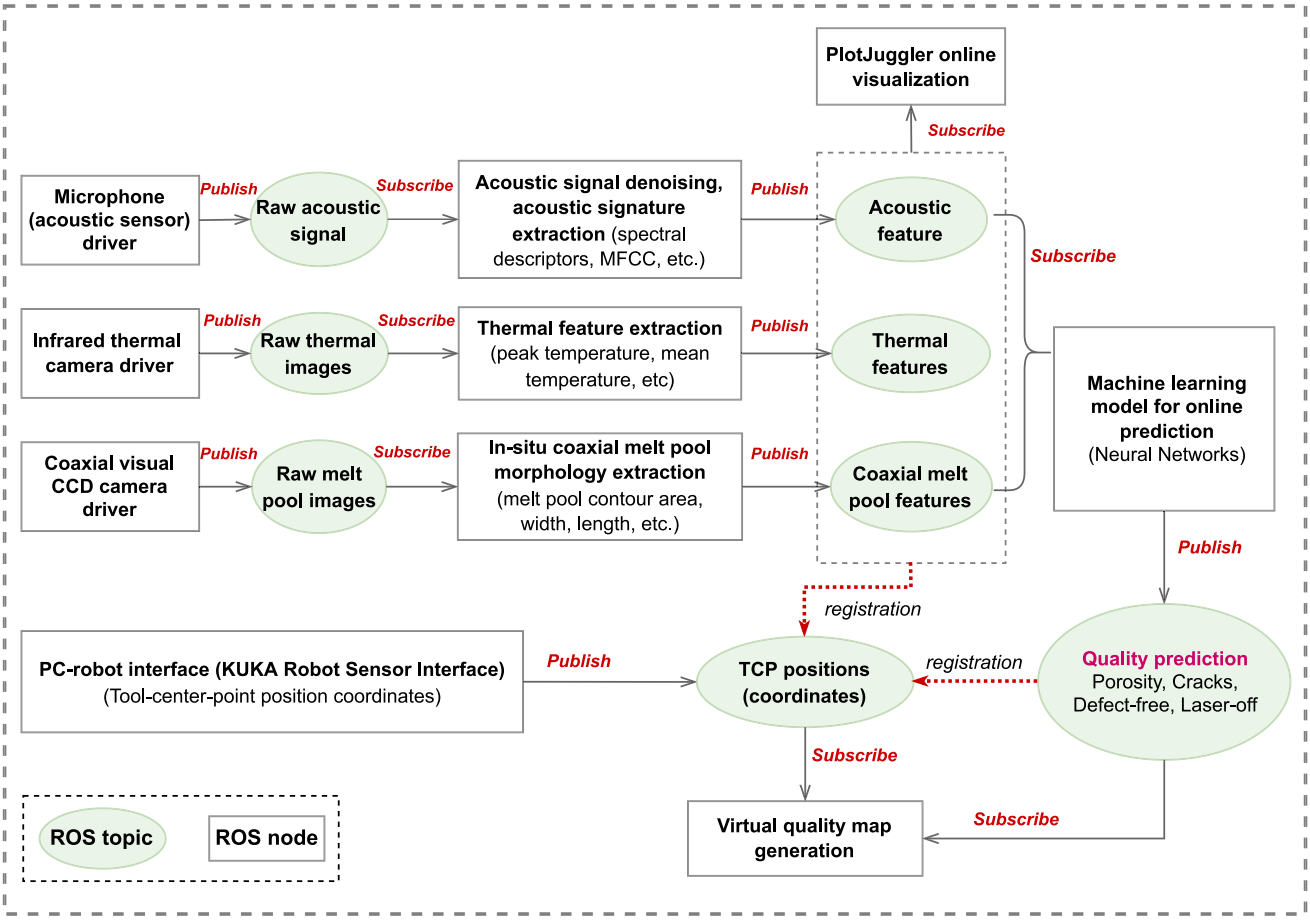


**Fig. 5.** ROS-based software architecture for multisensor in-situ monitoring, feature extraction, spatiotemporal feature registration, and defect prediction.

to the defective locations to remove the material based on the virtual quality map.

The Graphical User Interface (GUI) of the in-house developed software platform for multisensor monitoring is depicted in Fig. 6. The GUI can subscribe and visualize various key sensor features (e.g., melt pool

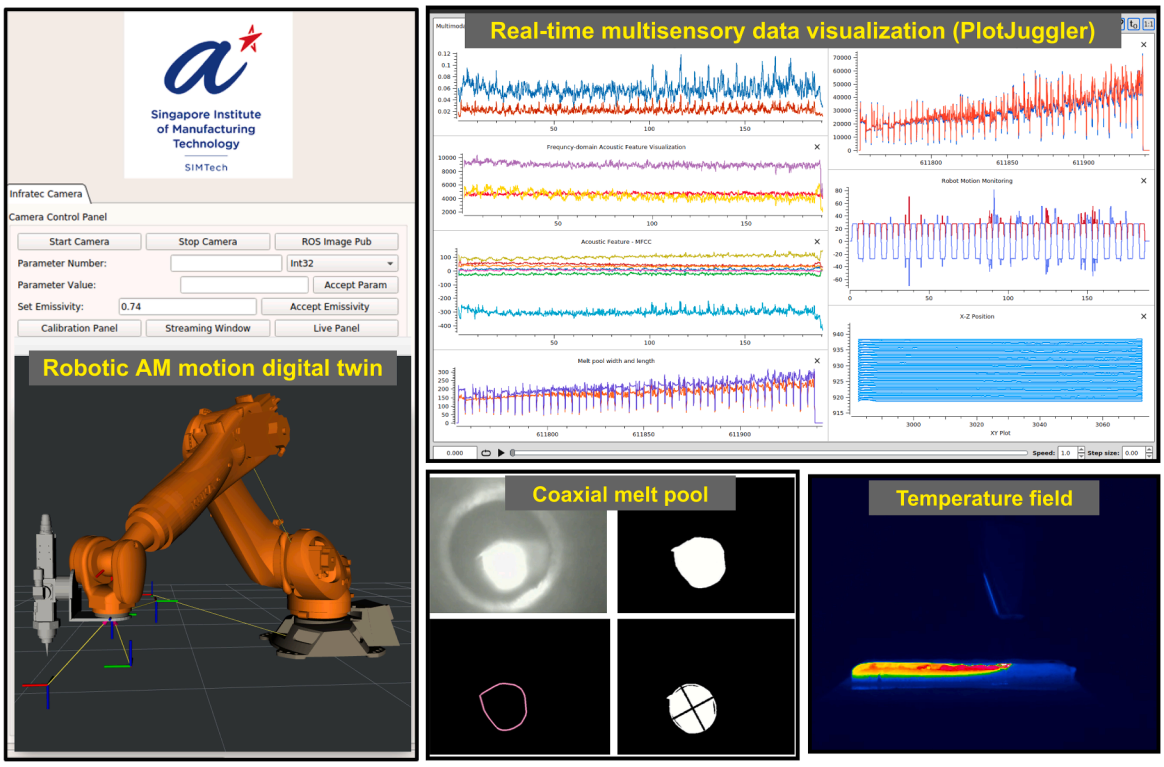


**Fig. 6.** GUI of the multisensor monitoring software platform for robotic L-DED process.

width, acoustic signal spectrum descriptors, robot motion, etc.) during the robotic L-DED process.

### 3.3. Multisensor monitoring and feature extraction

In this sub-section, we introduce the multisensor feature extraction techniques. The extracted features are used for spatiotemporal data fusion and localized quality prediction.

#### 3.3.1. Coaxial melt pool geometry monitoring

The coaxial melt pool geometric features can represent the melt pool heat transfer state and process stability. Fluctuations in the melt pool geometry could indicate localized heat accumulation, potential build anomalies and defects [56]. We adopted a similar method as presented by Knaak et al. [57] to extract melt pool morphological information. Melt pool width and length represented by a Minimum Oriented Bounding Boxes (OBB) and an ellipse were chosen as key features. In addition, we extracted the melt pool contour area, convex hull area, centroid positions, and central moments to describe melt pool dynamics. The definitions of these features are explained in Table 2. All the feature extractions were implemented by the OpenCV C++ library.

Fig. 7 demonstrates the coaxial melt pool image processing for feature extractions. The raw melt pool image (Fig. 7(a)) was binarized (Fig. 7(b)). Then various features can be visualized in Fig. 7(c)-(f). Fig.s 8(a)-(d) shows time-series plots of key coaxial melt pool geometric features when printing a single-bead wall structure. In Fig. 8(a), the ellipse width and maximum contour area shared a similar trend. When printing the initial layers, the melt pool area and width dropped, then increased and became less stable over time. A similar trend can be seen for convex hull area, $\mu_{20}$, $\mu_{02}$ and rectangle bounding box width and length. This was due to the change in the heat conduction mechanism that occurred during the deposition process (i.e., less material to conduct the heat as the part was built higher). The localized heat accumulation caused material vaporization and the formation of cracks and gas-induced pores, which were regarded as abnormal printing states. The third-order central moment of the melt pool ($\mu_{03}$) in Fig. 8(c) exhibited a high sensitivity to process anomaly, where the process transiting from the stable to the unstable zone can be observed from its dynamic fluctuations.

**Table 2**
List of coaxial melt pool geometric features

| Feature name | Mathematical expression/definition | Description |
|---|---|---|
| Melt pool contour area | $m_{00} = \sum_x \sum_y I(x,y)\Delta A$ | $0^{th}$ order moment, where $I(x,y)$ represents pixel intensities |
| Melt pool centroid position | $\bar{x} = \frac{m_{10}}{m_{00}}; \bar{y} = \frac{m_{01}}{m_{00}}$ | $1^{st}$ order moment represents the centre of gravity (COG) |
| Central Moments ($\mu_{ji}$) | $\mu_{ji} = \sum_x \sum_y I(x,y)\cdot(x-\bar{x})^j \cdot (y-\bar{y})^j$ | Moment of probability distribution about the COG, where $(\bar{x}, \bar{y})$ is the COG |
| Convex hull area | $C \equiv \{ \sum_{j=1}^{N} \lambda_j p_j : \lambda_j \geq 0$ for all $j$ and $\sum_{j=1}^{N} \lambda_j = 1 \}$ | The smallest convex set that contains the melt pool contour |
| Bounding rectangle width and length | Minimum Oriented Bounding Boxes (OBB) algorithm [58] | Bounding rotated boxes for contours |
| Ellipse width and length | $\frac{(x\cos\alpha + y\sin\alpha)^2}{a^2} + \frac{(x\sin\alpha - y\cos\alpha)^2}{b^2} = 1$ | Calculates the ellipse that fits the melt pool contour in a least-square sense |

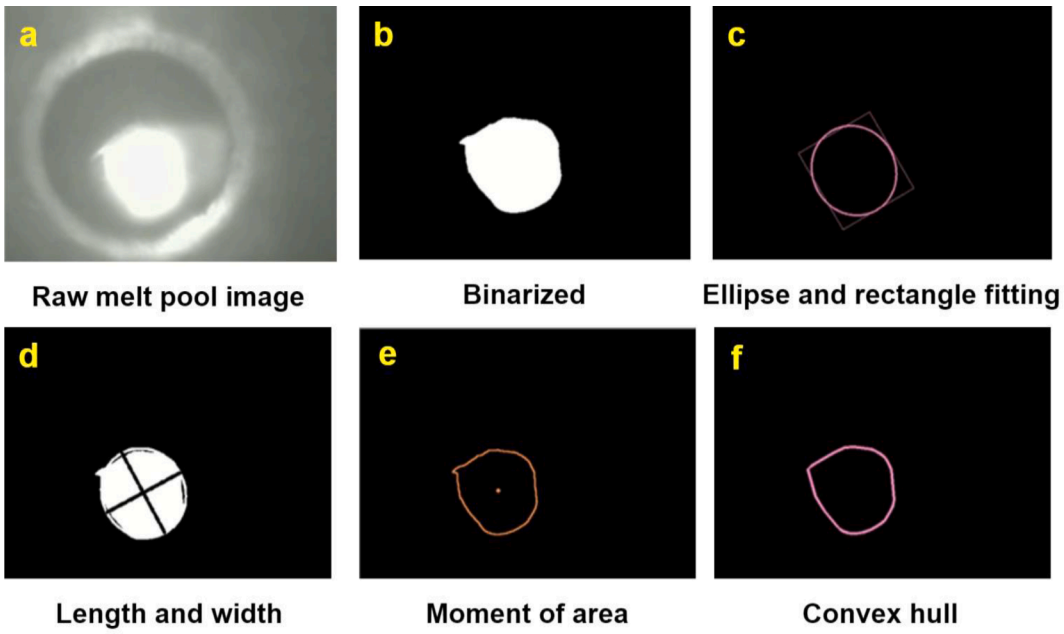


**Fig. 7.** Coaxial melt pool image processing and geometric feature extraction.

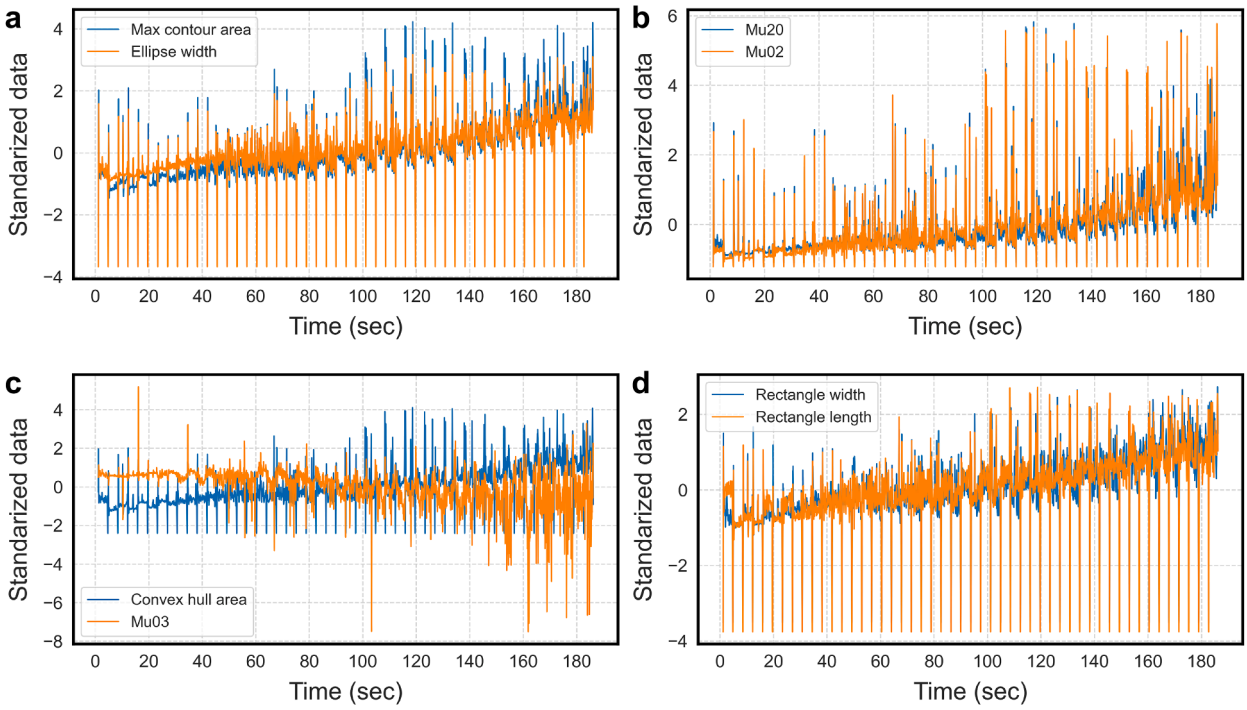


**Fig. 8.** Time series plots of coaxial melt pool geometric features when printing a single bead wall structure. (a) Max contour area and fitted ellipse width of melt pool. (b) Melt pool second moment of area (note: Mu20 means $\mu_{20}$, Mu02 means $\mu_{02}$ in the figure), (c) Melt pool convex hull area and third moment of area ($\mu_{03}$). (d) Melt pool width and length fitted by a minimum bounding rectangle box.

### 3.3.2. *In-situ acoustic monitoring*

Acoustic-based monitoring methods provide distinct advantages over vision-based sensing, such as adjustable sensor setup and lower hardware costs. Recently, an acoustic denoising technique was proposed, which can significantly reduce the noise and enhance the defect prediction performance for L-DED [39]. The denoised signal was used to extract features and perform data analysis. As listed in Table 3, several spectral descriptors and Mel-Frequency Cepstral Coefficients (MFCCs) were selected as key acoustic features based on our previous research [40]. Fig. 9 visualizes the time-domain variations of the key acoustic characteristics collected from L-DED of a single bead wall structure. Interestingly, the MFCC0 and MFCC1 acoustic features in Fig. 9(a) exhibited the same trend as the coaxial melt pool width and area in Fig. 8 (a). The value dropped for the initial layers and then steadily climbed as the fluctuations increased. This is also true for spectral bandwidth and flatness in Fig. 9(c). Nevertheless, the MFCC2, MFCC3, spectral centroid and variance had an inverse association with melt pool size and width (i.e., initially increase, then gradually decrease), as seen in Fig.s 9(b) and

**Table 3**
List of acoustic features and mathematical definitions

| Feature name | Mathematical expression | Description |
|---|---|---|
| MFCCs | $\boldsymbol{C}_{(x(t))} = F^{-1}[\log(F[x(t)])]$ | Cepstrum of a signal $x(t)$. $F$ represents the Fourier transform function, and $F^{-1}$ is inverse Fourier transform. The number of MFCCs is set to 12. (i.e., frequency bands are equally spaced on the Log-scale). |
| Spectral centroid (SC) | $SC_t = \frac{\sum_{n=1}^{N} m_{t(n)} \cdot n}{\sum_{n=1}^{N} m_{t(n)}}$ | Centre of gravity (COG) of the magnitude spectrum (Weighted mean of the frequencies) |
| Spectral bandwidth (SBW) | $SBW_t = \frac{\sum_{n=1}^{N} \lvert n - SC_t \rvert \cdot m_{t(n)}}{\sum_{n=1}^{N} m_{t(n)}}$ | Weighted mean of distance of frequency bands from SC |
| Spectral flatness (SF) | $SF_t = \frac{(\prod_{n=1}^{N} m_{t(n)})^{\frac{1}{n}}}{\frac{1}{n}\sum_{n=1}^{N} m_{t(n)}}$ | The ratio of the geometric mean of the spectrum to the arithmetic mean of the spectrum |
| Spectral variance | $\boldsymbol{\mu}_2 = \sqrt{\frac{\sum_{n=1}^{N} (n - SC_t)^2 m_{t(n)}}{\sum_{n=1}^{N} m_{t(n)}}}$ | The standard deviation around the spectral centroid. |
| Spectral skewness | $\boldsymbol{\mu}_3 = \frac{\sum_{n=1}^{N} (n - SC_t)^3 m_{t(n)}}{(\boldsymbol{\mu}_2)^3 \sum_{n=1}^{N} m_{t(n)}}$ | The third-order moment of spectrum, measuring the symmetry around the centroid. |
| Spectral entropy (H) | $H_t = \frac{-\sum_{n=1}^{N} m_t(n) \cdot \log(m_t(n))}{\log(N)}$ | Shannon entropy of the power spectral density (PSD). |

(d). This finding suggests that, like vision features, in-situ acoustic data may be capable of describing process stability and defect occurrences that are previously represented by melt pool width in most research.

### 3.3.3. Temperature field monitoring

Temperature field data from printed parts can be used to identify potential process anomalies. The emissivity value for the commercial C300 maraging steel was set to 0.5 for the entire process prior to extracting the temperature features. Although the true temperature profile cannot be accurately measured due to emissivity differences in material composition, phase, and temperature, the time-series thermographic images can reflect the general trend and fluctuations of the temperature values during the process. In this study, the melt pool temperature was not measured, since the liquidus molten pool had a different emissivity value than the solidified region. Instead, we captured the temperature field data for the entire printed single-bead wall structure (i.e., the ROI was defined as the area that contains the entire part). The thermal camera was perpendicular to the printed wall, capturing the entire part temperature inside its field of view. As the essential temperature field features, we extracted the peak temperature, mean temperature, temperature variance, and standard deviation within ROI, as defined in Table 4. The thermal properties of the single-bead wall structure are shown in Fig. 10. During the initial layers, the peak temperature, temperature variance, and standard deviation steadily increased before approaching a steady state. The mean temperature, on the other hand, increased gradually with the height of the part. This observation demonstrates the changes in the heat conduction mechanism when depositing a single bead wall structure, where heat was conducted to the base plate when printing the initial layers and conduction changed to 2D when the part was built higher, eventually

**Table 4**
List of temperature field features and mathematical definitions

| Feature name | Mathematical expression/ definition | Description |
|---|---|---|
| Peak temperature | Highest temperature value in the current timestamp | Peak temperature within ROI |
| Mean temperature | $\mu = \frac{\sum_{i=1}^{n} x_i}{N}$ | Mean temperature value within ROI |
| Temperature standard deviation (std) | $\sigma = \sqrt{\frac{\sum (x_i - \mu)^2}{N}}$ | Temperature standard deviation within ROI |
| Temperature variance (span) | $Var[X] = S^2 = \frac{\sum_{i}^{N} (X_i - \mu)^2}{(N-1)}$ | Temperature variance (span) within ROI |

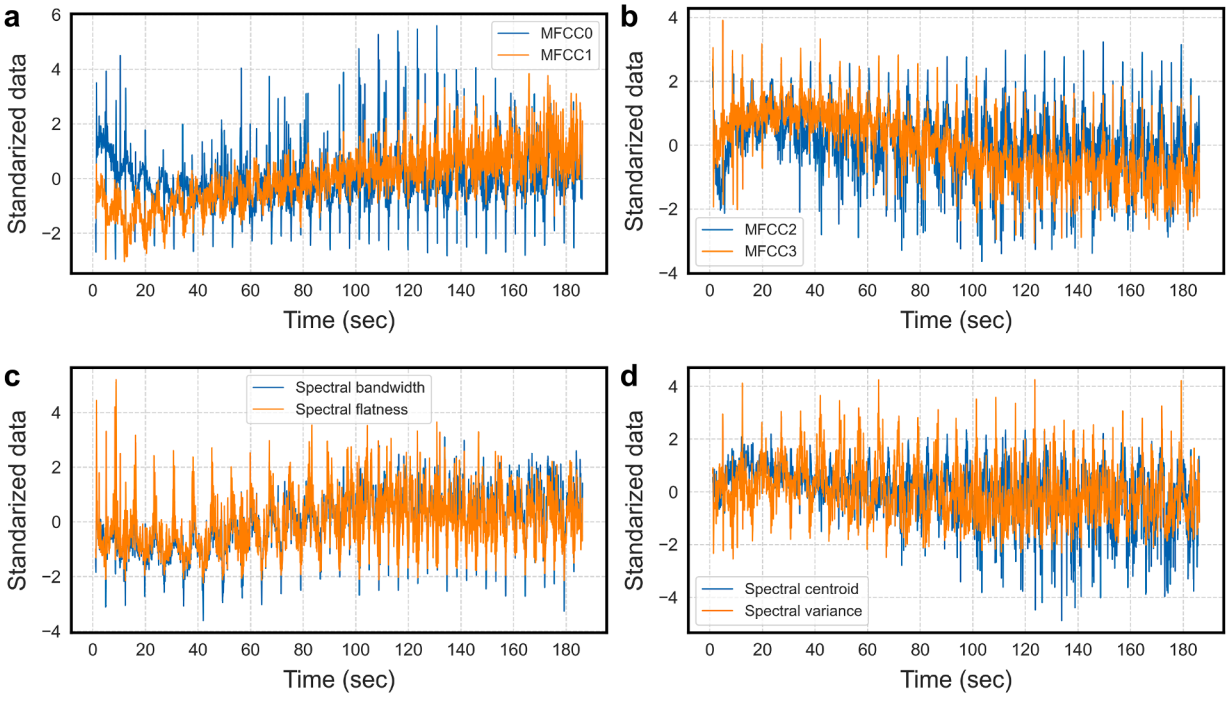


**Fig. 9.** Time series plots of acoustic features when printing a single bead wall structure. (a) MFCC0 and MFCC1, representing cepstrum energy in the low frequency band (0 Hz - 1024 Hz). (b) MFCC2 and MFCC3, representing cepstrum energy in the middle frequency band (1024 Hz - 4096 Hz). (c) spectral bandwidth and spectral flatness. (d) spectral centroid and variance. (Note: the acoustic signal is denoised using method presented in [39] before feature extractions.).

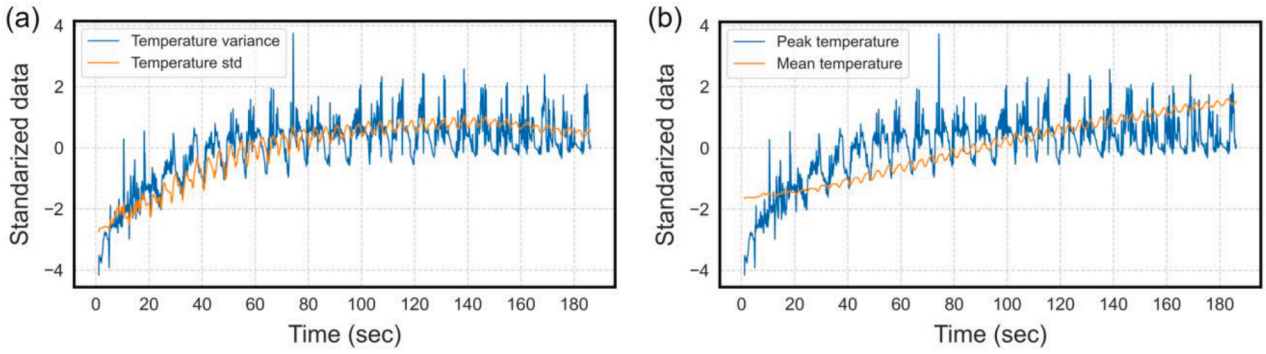


**Fig. 10.** Time series plots of temperature field features when printing a single bead wall structure. (a) Temperature variance and standard deviations within ROI, (b) Peak temperature and mean temperature.

reaching a steady state.

The extracted key features from the vision, acoustic and thermal sensing modalities were synchronized and registered with the real-time robot TCP position data retrieved from the robot controller. Subsequent ML model prediction outputs were also tagged with TCP positions (i.e., the x,y,z coordinates), allowing for location-specific quality predictions. The details on spatiotemporal data fusion are explained in the next subsection.

### 3.4. Spatiotemporal data fusion

After extracting features from multisensor inputs, the features were spatiotemporally registered with robot TCP positions for location-specific quality mapping. All features from different sensing modalities were extracted and collected at the same time stamp using the ROS-based software platform. Fig. 11 illustrates the synchronization and registration of multisensor features, ML prediction outcomes, and robot TCP positions. Although each sensor had a different acquisition frequency (raw acoustic image at 30 Hz, raw acoustic signal at 44,100 Hz, and raw thermal image at 30 Hz), the extracted features for all three sensing modalities were made available at a consistent frequency of 30 Hz. During each 33 ms period, key features of the acoustic signals were extracted, including both time-domain and frequency-domain information, such as spectral descriptors and MFCCs. These acoustic time-frequency representations were able to effectively depict the acoustic events that occurred within the interval without any loss of information. In order to synchronize the sensor features that were published from different channels, we implemented the Approximate Time Synchronizer algorithm from the ROS message filter module [59]. Messages from various sensing modalities can be aligned using the Approximate Time Synchronizer based on their respective time stamps. The algorithm identified the most recent message among the topic-specific queues as a reference point within a defined interval (i.e., the prediction window as illustrated in Fig. 11). These messages were then synchronized within a specified threshold, which was 33 ms. The ML model can then make a prediction in each prediction window using the synchronized multi-sensor features from different channels. Additionally, the features and ML prediction outputs can also be aligned and registered with TCP positions based on their time stamps using the Approximate Time Synchronizer algorithm.

In this study, we did not seek absolute synchronization and registration between the multisensor feature, ML prediction, and TCP position. Since computer program execution times varied slightly, it was impractical to ensure that all messages were published at the exact time stamps. While there was a small latency (<30 ms) due to approximate synchronization, which could cause the predicted defects to be slightly delayed (< 1 mm) compared to the actual defect location, it was sufficient for real-world applications because we only need to know the approximate boundaries (or layers) of the defective regions. Furthermore, the prediction delay induced by computing (e.g., inference time for the trained ML model) was also omitted because it was on the order of microseconds, which had little influence on real-word application performance.

Fig. 12 depicts feature-level digital twins of the L-DED process after the multisensor features are registered spatiotemporally with the robot TCP position data. The interior quality of the part was examined under optical microscope (OM) image, as shown in Fig. 12. The OM image reveals large keyhole pores in the upper layers, cracks in the middle

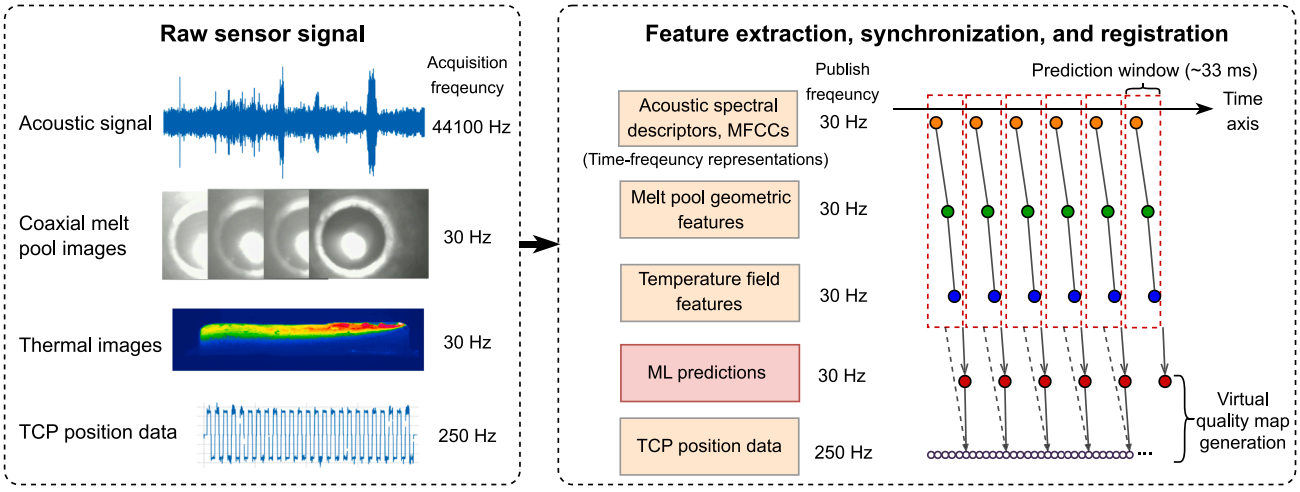


**Fig. 11.** Illustration of synchronization and registration between multisensor features, ML predictions and TCP positions.

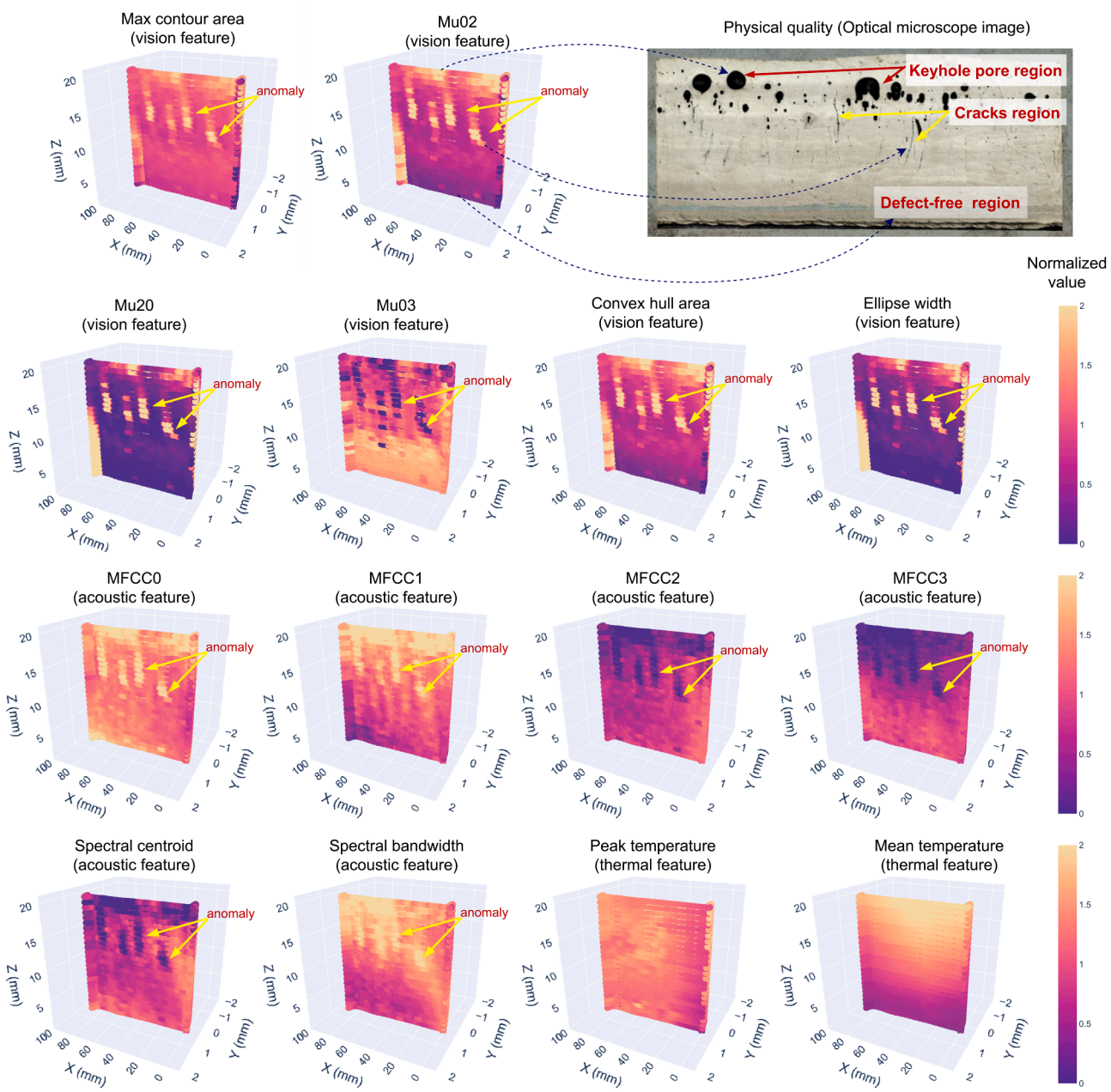


**Fig. 12.** Spatial visualization of multisensor features and physical quality observed from OM photo.

layers, and a defect-free zone in the lower layers of the part. In particular, two macroscale cracks can be observed in the centre of the sample. These defective spots can be matched with the multisensor feature values as shown in the spatial plots in Fig. 12. For example, abrupt increases in melt pool width (marked as "anomalies") in the middle layers were linked to the macro-scale cracks observed from the OM image, while larger melt pools in the top layers could reflect keyhole porosity. It may also be seen that different sensing modalities shared similar patterns within the part volume. For example, the acoustic signal's MFCCs features, spectral centroid, and bandwidth characteristics exhibited abrupt value changes at the same locations that correspond to the cracks (marked as "anomalies"), as seen in coaxial melt pool features. The temperature field feature, on the other hand, was unable to identify such anomalies, indicating its limited effectiveness in distinguishing cracking defects. Nonetheless, all features from different sensing modalities followed a similar trend, with the value increasing (e.g., melt pool ellipse width, contour area, peak temperature) or decreasing (e.g., MFCC2, MFCC3, spectral centroid, Mu03) with time and layer height, corresponding to localized heat accumulation and quality deterioration.

The fused multimodal dataset was used to train supervised ML models that predict the defect occurrences. An exploratory data analysis (EDA) was conducted prior to ML model training to further analyse the multimodal dataset and provide guidance for ML model selections, which will be shown in the next sub-section.

### 3.5. Exploratory data analysis

Finding correlations between critical multisensor features prior to incorporating them into ML models for quality classification can determine the complexity of the ML model required for defect prediction. Exploratory data analysis (EDA) is conducted on in-situ extracted key multisensor feature data. The whole dataset consists of a total of 27 features from three sensing modalities: 4 temperature field features from infrared thermal sensing, 9 features from coaxial melt pool geometric

features, and 14 features from the denoised laser-material interaction sound. Fig. 13 depicts Spearman's correlation matrix [60] for the collected multimodal dataset. The value ranges from -1 to 1, with 1 indicating the most positive correlation, -1 indicating the highest negative correlation, and 0 indicating no correlation. The correlations between the features from different sensing modalities were surprisingly strong. Traditionally, melt pool width has been the most common quality indicator used to represent the process's stability. According to Fig. 13, a number of characteristics from acoustic sensing modalities had a strong correlation with the melt pool width ("ellipse width"). For example, MFCC0, MFCC1, and spectral bandwidth from acoustic sensing modality had a strong positive correlation (>0.7) to melt pool width, whereas MFCC2 and MFCC3 exhibited a strong negative correlation (<-0.7). This finding reveals that when melt pools reach unstable phases in which the width grows as the parts are built higher, the acoustic signal energy in the middle-frequency bands (MFCC2, MFCC3) decreases while it increases in the low-frequency bands (MFCC0, MFCC1). This also demonstrates the potential of acoustic sensing for the L-DED process, where acoustic features can be used as quality indicators for in-situ monitoring and closed-loop feedback control applications. Furthermore, as shown in Fig. 14, we used four dimensionality reduction techniques to analyse the multidimensional dataset:

(1) Linear Discriminant Analysis (LDA): a dimensionality reduction technique for finding a linear combination of features that maximally separates different classes in a dataset. LDA can handle large datasets efficiently. Fig. 14(a) depicts the LDA projection on 2D space, which indicates separable clusters for each of the output labels. The "laser-off" signal can be easily distinguished from the others. "Keyhole pore" can also be differentiated from defect-free regimes, whereas cracks are much more difficult to isolate.

(2) Principal Component Analysis (PCA): a dimensionality reduction technique that decompose the multivariate dataset into a set of orthogonal components, capturing the key structure of the data. PCA is sensitive to data scaling and cannot capture nonlinear relationships in the data. Fig. 14(b) demonstrates that PCA is not as effective as LDA in distinguishing classes, yet "laser-off" data can still be easily separated from the other classes.

(3) Isometric Mapping (Isomap): a nonlinear dimensionality reduction method that uses geodesic distances to preserve a dataset's structure and lower its dimensionality. Isomap shows a similar separation effect as LDA.

(4) T-distributed Stochastic Neighbour Embedding (t-SNE): a nonlinear dimensionality reduction method that preserves the local structure of the data. t-SNE is well-suited for datasets with

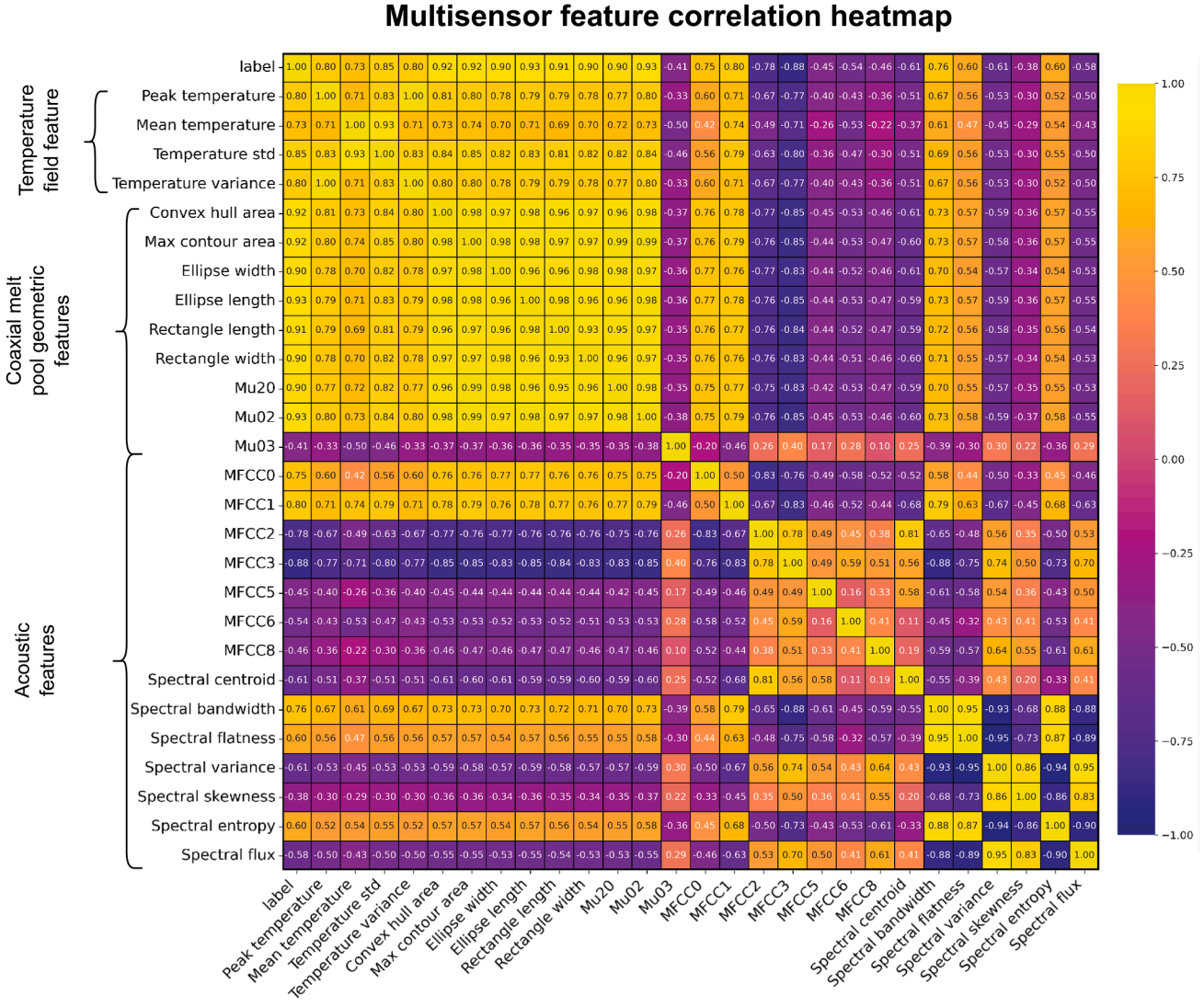


**Fig. 13.** Spearman's correlation heatmap of key multisensor features and output class (i.e., '0′ - laser-off, '1′ - defect free, '2′ - cracks, '3′ - keyhole pores).

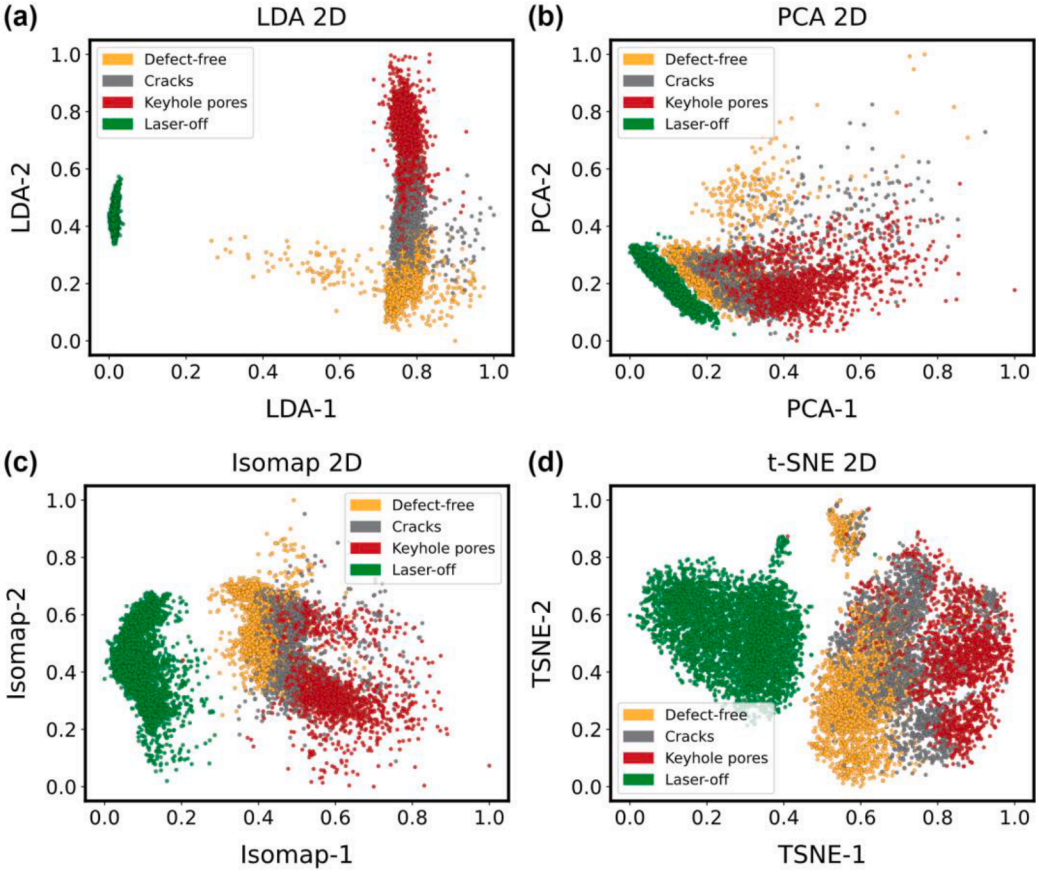


**Fig. 14.** Low-dimensional visualization of multisensor features by different dimensionality reduction techniques: (a) Linear Discriminant Analysis (LDA), (b) Principal Component Analysis (PCA), (c) Isometric Mapping (Isomap), (d) T-distributed Stochastic Neighbour Embedding (t-SNE).

complex structures. t-SNE exhibits a similar separation effect as LDA and Isomap.

The dimensionality reduction results in Fig. 14 reveal that the multidimensional dataset can form distinct clusters in low-dimensional space. In particular, the signals from the "laser-off" can be distinguished from the others the most clearly. The "defect-free" category is unique from "keyhole pore", with very little overlap. The "crack" category, on the other hand, has a high degree of overlap with the "defect-free" and "keyhole pore" categories, implying that the crack signal may be difficult to distinguish from the other classes. The above exploratory data analysis proves that a supervised ML model is feasible to classify different quality using the multidimensional dataset. However, it might be challenging to accurately predict the crack occurrences (i.e., misclassifying the "cracks" as "keyhole pores" or "defect-free" is possible). Therefore, selecting ML algorithms with hyperparameters that can handle high dimensional and non-linearly separable data is required, which will be shown in the next sub-section.

### 3.6. Machine learning models for localized quality prediction

Seven supervised ML algorithms were evaluated in this study to predict L-DED defects (cracks and keyhole pores) using the multimodal dataset described in the previous sections. The seven ML algorithms were Support Vector Machine (SVC), K-Nearest-Neighbour (KNN), Decision Trees (DT), Random Forest (RF), Neural Network (NN), Logistic Regression (LR), and Gradient Boosting Trees (GB). The open-source Scikit-learn Python package [61] was used to implement the algorithms for training and testing. The whole multimodal fused dataset comprised of 292,200 data points that correspond to each robot's TCP position at recorded timestamps. Each data point was labelled with a ground truth quality category based on OM image observations. The dataset was divided into a training set and a testing set in a ratio of 8:2. The grid search approach was used to optimize hyperparameters for ML models. The grid search is an extensive search methodology that compares all feasible hyperparameter value combinations. K-fold cross-validation (k=10) was conducted to assess performance throughout each iteration of the hyperparameter tuning procedure. The k-fold cross-validation is performed for each of the k-folds, and the final accuracy score is the average of the k-accuracy values. The hyperparameter combination with the highest cross-validated score is chosen at the end of the grid search. Table 5 shows the investigated hyperparameter ranges and the final optimum hyperparameters for each ML model. For testing, seven ML algorithms with optimal hyperparameters after training and tuning are employed. Section 4 will present and discuss the model performance evaluation results.

## 4. Results and discussion

The performances of ML classification models are examined and discussed in this Section. The ML model with the highest prediction accuracy is chosen to be implemented on the proposed MFDT framework. The predicted quality values can be registered with the position data to achieve location-specific quality prediction. This Section shows the virtual quality map that registers the quality prediction outcomes with the location information.

### 4.1. Model evaluation

To validate the effectiveness of the proposed multisensor fusion over

**Table 5**
Optimal hyperparameters and their range studied in our ML models for multisensor-based quality prediction

| Models | Hyperparameters | Optimal values | Range studied |
|---|---|---|---|
| SVM | Kernel | RBF | ['linear', 'rbf', |
| | Regularization parameter | 1000 | 'sigmoid'] |
| | (C) | 0.01 | [1, 10, 100, 1000, |
| | Kernel coefficient (γ) | | 1500] |
| | | | [1e-2,1e-3, 1e-4] |
| KNN | Number of neighbours | 10 | [4, 5, 6, 8, 10, 20, 50] |
| | Weight function | Distance | ['uniform', 'distance'] |
| DT | Minimum sample split | 3 | [2, 3, 4, 5, 6] |
| | Maximum depth of the tree | 10 | [2, 5, 10, 20, 30] |
| RF | Minimum sample split | 2 | [2, 3, 4, 5, 6] |
| | Number of tree estimators: | 300 | [2, 5, 10, 100, 300, 500] |
| | Maximum depth of the tree | 50 | [2, 5, 10, 50, 100] |
| NN | Number of neurons | (16, 64, 256) | [16, 32, 64, 256, 512] |
| | Alpha | 0.1 | [1e-3, 1e-2, 1e-1] |
| | Activation function | 'ReLU' | ['tanh', 'ReLU', |
| | | | 'sigmoid'] |
| LR | Regularization (C) | 1.0 | [1.0, 0.1] |
| | max iteration | 500 | [500, 1000] |
| GB | Number of estimators | 500 | [10, 100, 500, 1000] |

the traditional single-sensor-based defect prediction methods, ML models were trained and tested on both the multisensor fused dataset and the dataset with only single sensing modality features provided (i.e., trained with only acoustic features, only vision features, or only thermal features). Both the multisensor fusion dataset and the single sensing dataset were randomly split into a training set and a test set to assess the model performance. Since the data distribution was imbalanced, the stratified random split was used to divide the training and test datasets. The ratio of the train to test is 8:2. The total multisensor fused dataset consisted of 29,200 data points corresponding to each robot TCP location at recorded time stamps for all samples. To demonstrate its viability and repeatability, all of the ML model evaluations reported in this paper were averaged over five runs, with standard deviations marked as error bars. The evaluation metrics for the ML classification models are described as follows:

- Accuracy score: the accuracy score is the total correctly predicted sample divided by total prediction, which can be defined as:

$$Accuracy = \frac{TP + TN}{TP + FP + TN + FN} \tag{1}$$

where TP is true positive, TN is true negative, FN is false negative, and FP is false positive. The total accuracy score evaluates the model's overall performance in multiclass classification. The test accuracy of the ML models trained on the multisensor fusion dataset significantly outperformed the models trained using single sensing modality features, as shown in Fig. 15(a). Among all classifiers, the NN classifier scored the highest overall accuracy (95.6%) and was chosen to be deployed on the MFDT software platform. Furthermore, it can be observed that the acoustic-based sensing modality achieved almost the same prediction accuracy as the vision-based sensing approach. Thermal sensing was less accurate than vision and acoustic sensors in predicting quality.

- Receiver Operating Characteristics (ROC) curve: the x-axis of ROC plots is the false positive rate (FPR) (i.e., percentage of FP out of the negatives), and the y-axis is the true positive rate (TPR) (i.e., percentage of true positives out of positives). The definitions of them are:

$$FPR = \frac{FP}{FP + TN} \tag{2}$$

$$TPR = \frac{TP}{TP + FN} \tag{3}$$

The ROC curve assessed the model's performance for classification problems at various threshold levels. Better performance was represented by the curve approaching the upper-left corner (i.e., FPR approaches to 0, and TPR approaches to 1). As demonstrated in Fig. 16, the NN classifier trained on the multisensor fusion dataset outperformed the NN trained on single sensing modalities in terms of the ROC curve for each class.

- Aera under the ROC (AUC-ROC) scores: The AUC-ROC score represents the degree of separability. It tells how much the model is capable of distinguishing between classes. The higher the AUC, the better the model is at predicting the true positives and true negatives. As shown in Fig. 16, NN trained on a multisensor fusion dataset achieved almost perfect AUC scores for each class, while those trained on single sensing features had significantly lower AUC-ROC scores (e.g., cracks predicted by the vision sensor has only 0.93 score). The comparison is shown in Fig. 15(b), where NN is the best classification model in terms of the AUC-ROC score.
- Confusion matrix: A confusion matrix is a type of contingency table with two dimensions ("ground truth" and "predicted") and the same

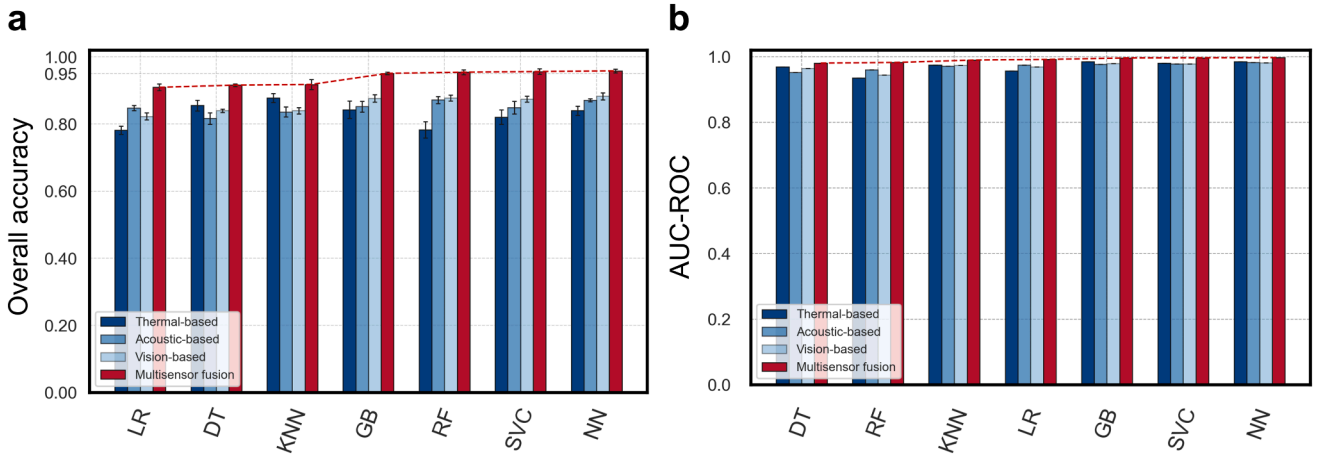


**Fig. 15.** Performance evaluation for multisensor fusion-based defect prediction in L-DED. (a) The overall test accuracy of seven supervised ML classifiers trained using single sensing modality features and multisensor fusion features. (b) AUC-ROC results of seven ML classifiers trained on single sensing modality features and multisensor fusion features.

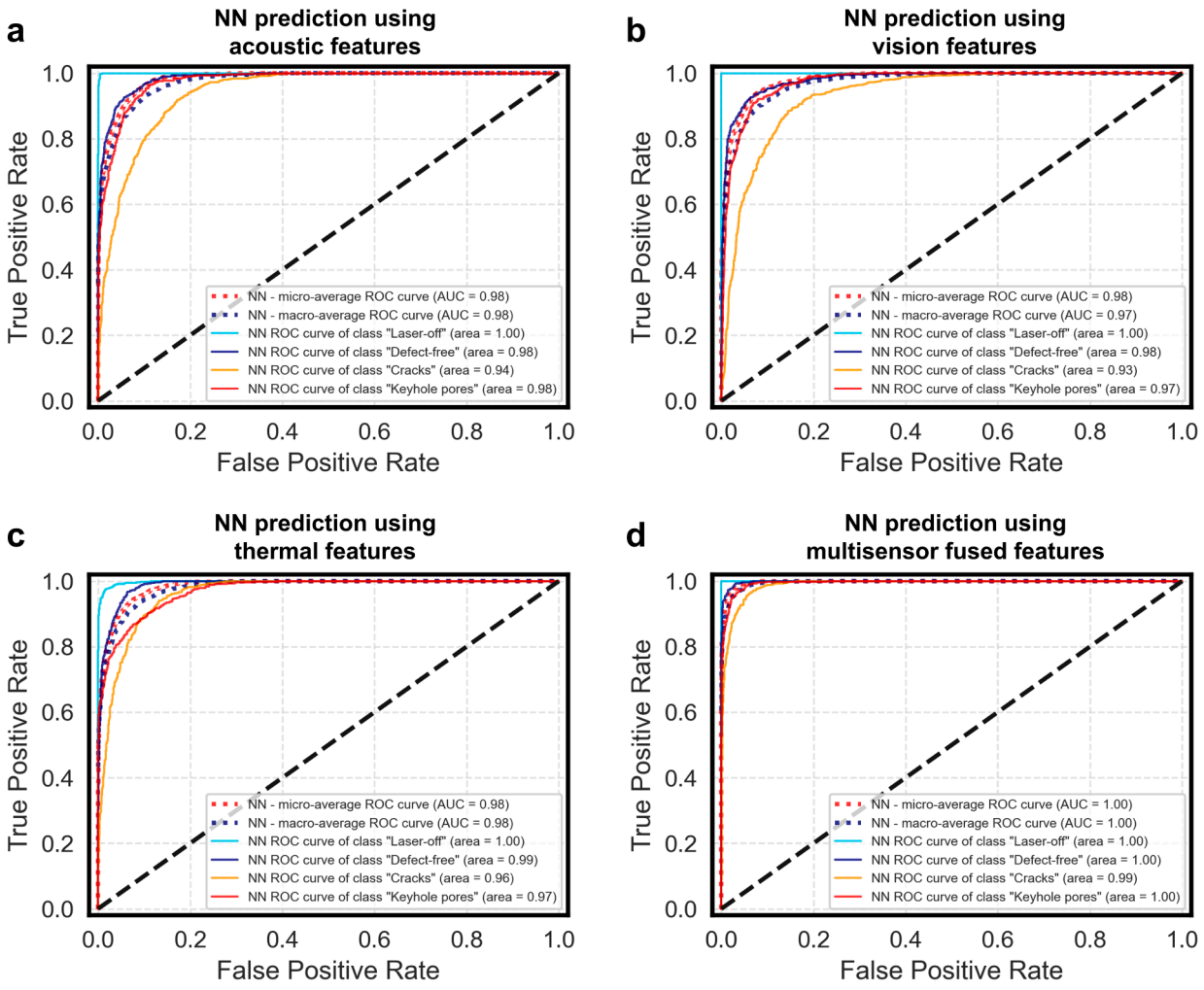


**Fig. 16.** Receiver operating characteristic (ROC) curves for the defect classification task by NN classifier trained on (a) acoustic features, (b) vision features, (c) thermal features, (d) multisensor fused features. The results demonstrate superior classification accuracy of the NN classifier trained using multisensor fusion than trained using single sensing modality.

sets of "classes" in both dimensions (each combination of dimension and class is a variable in the contingency table). It is a more comprehensive method of evaluating ML classifier performance because it can show which classes are incorrectly classified. Fig. 17 compares the confusion matrix for NN prediction using the multisensor fusion dataset versus the single sensing datasets. The NN trained on multisensor fusion had the best accuracy (89.6 %) in predicting the "cracks" class, while those trained on vision and acoustic-based sensing had only 75 % -76 % in crack prediction. The multisensor fusion also achieved significantly higher accuracy (94.3 %) for keyhole pore predictions, which is nearly 14.5% higher than utilizing vision-based sensing, 17.6% higher than acoustic-based sensing, and 21.2% higher than thermal-based sensing.

- False alarm rate: the actual non-defect region (including the 'laser-off' period and 'defect-free') predicted as defective (including 'cracks' and 'keyhole pores') is considered a false alarm. From the confusion matrix in Fig. 17, the multisensor fusion-based prediction achieved the lowest false alarm rate (4.4%) than the other single-sensing-based prediction (11% for vision-based, 8.4% for acoustic-based, and 8.4% for thermal-based).

### 4.2. Visualization of localized quality prediction

In this Section, the proposed MFDT capability is demonstrated by depositing a single-bead wall sample. The trained NN model was deployed in the software platform for localized quality prediction. The predicted quality result was made accessible through a ROS topic broadcast at a frequency of 30 Hz. At each time stamp, the predicted quality (i.e., 'laser-off,' 'defect-free,' 'cracks,' and 'keyhole pores') can be paired with real-time robot position coordinates, allowing for localized defect prediction. Fig. 18(a) shows the physical quality of the printed single-bead wall structure, with defect-free zones in the initial layers, cracks in the middle layers, and keyhole pores in the upper layers. In this research, we did not seek for individual defects detection. Instead, we predict the defective regions as shown in the in the Fig. 18 (a). If cracks or keyhole pores occurred in a 500 ms segment (approximately 12 mm neighbourhood), the entire signal for that region were labelled as "cracks" or "keyhole pores". Despite the fact that the OM image indicated certain gaps between the cracks and pores, such gaps were labelled with the same category as their neighbouring defect. The region-based data annotation is due to two reasons: (1) if the neighbouring region contains cracks or porosity, the overall region quality is poor. Regardless of how many cracks or pores exist, the entire region must be removed; (2) the gaps between the defects are extremely narrow (only around 1-2 mm). Defects are in close proximity to one another. As a result, identifying precise pores or cracks in the signal is extremely challenging. The quality in the neighborhood of a defect is assumed to belong to the same defective category in region-based data annotation, which avoids mismarking and enhances model robustness to certain multisensor signal misalignment. The length of the region (500 ms

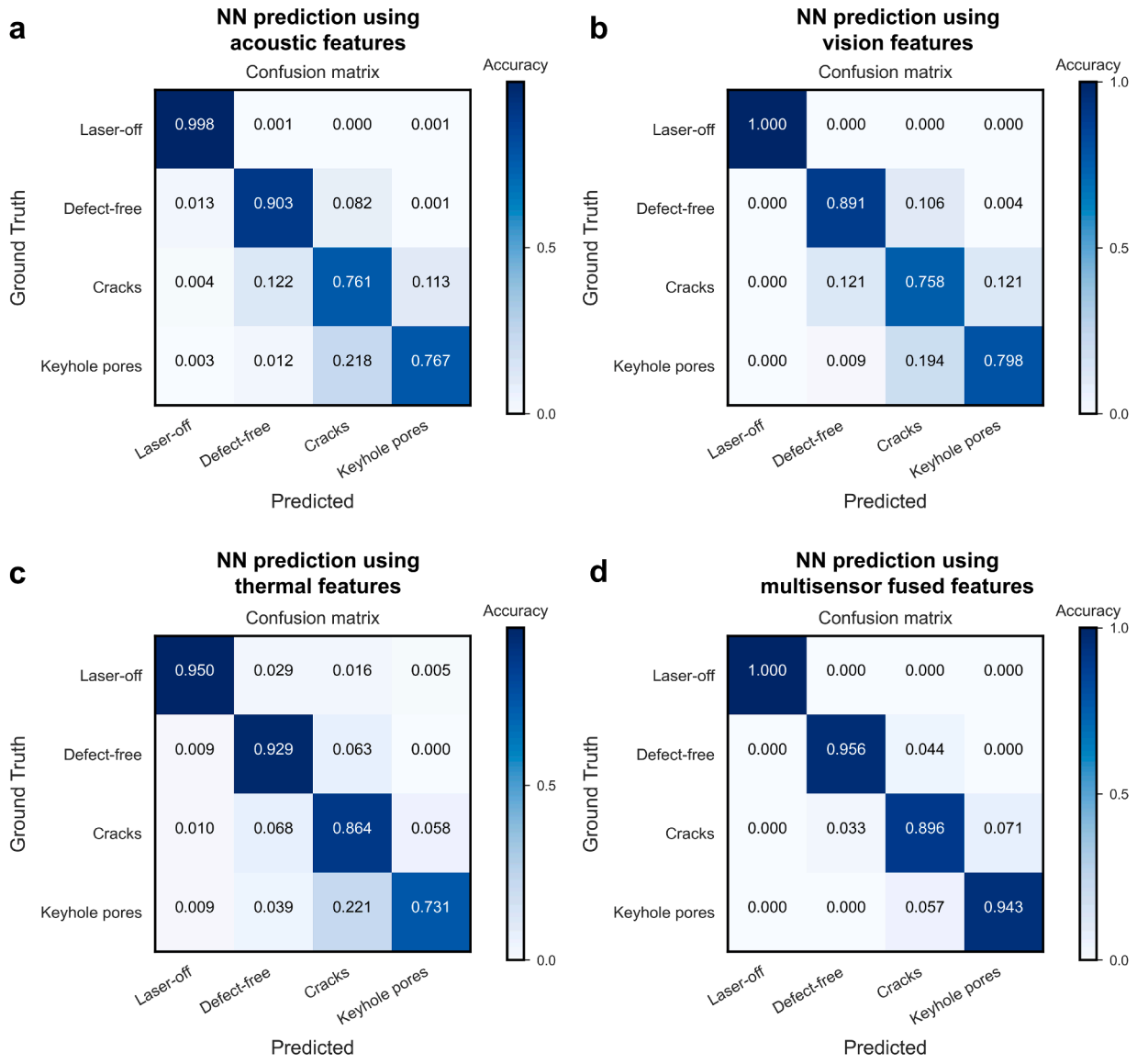


**Fig. 17.** Confusion matrix for the defect classification task for NN classifier trained on (a) acoustic features, (b) vision features, (c) thermal features, (d) multisensor fused features. The results demonstrate superior classification accuracy of the NN classifier trained using multisensor fusion than trained using single sensing modality.

segment) was determined by trial and error as a compromise between ML model accuracy and spatiotemporal resolutions.

A virtual quality map was constructed by combining the predicted quality values and location information, as shown in Fig. 18(b)-(e). The "laser-off" period occurred at the toolpath's turning corners and was hence not shown in Fig. 18. Fig. 18(b) depicts the virtual quality map predicted by NN utilizing multisensor features (all vision, acoustic, and thermal features combined), which closely matched the physical quality values acquired from OM. There were very few locations that were incorrectly categorized by the multisensor fusion-based prediction. However, as shown in Fig.s 18(c)-(e), the virtual quality maps predicted using only vision, acoustic or features performed significantly worse. The vison-only and acoustic-only predictions tended to exaggerate defect occurrences (i.e., predicting a defect-free zone as flawed), whereas the thermal-only prediction tended to underestimate defect occurrences. Therefore, the multisensor fusion is proved to be a more reliable and robust approach compared to single-sensor monitoring methods.

The proposed MFDT framework can perform localized quality prediction in the robotic L-DED process. However, it is worth noting that the complete digital twin comprises not only the mapping of physical entities in the virtual space but also the control of physical systems based on the predicted outcomes in the virtual space. Our work presented in this paper focuses primarily on the first half of the digital twin (i.e., mapping physical entities in the virtual space). Although the other half of the digital twin (i.e., controlling physical entities) is not the key focus in this study, it can also be accomplished based on the proposed MFDT framework. Physical process control can be achieved in the following three ways, which is part of our on-going research:

i The machine learning (ML) model makes a localized quality prediction every 30 milliseconds and issues warning signals to the user interface of our L-DED system when defects are detected. The process can be paused automatically to prevent further quality deterioration once warning signals are received.
ii In addition to categorical defect prediction, the ML model can predict the likelihood of defect occurrence. This defect occurrence probability can be used as a feedback signal for closed-loop process adjustment. For example, when the probability of a defect

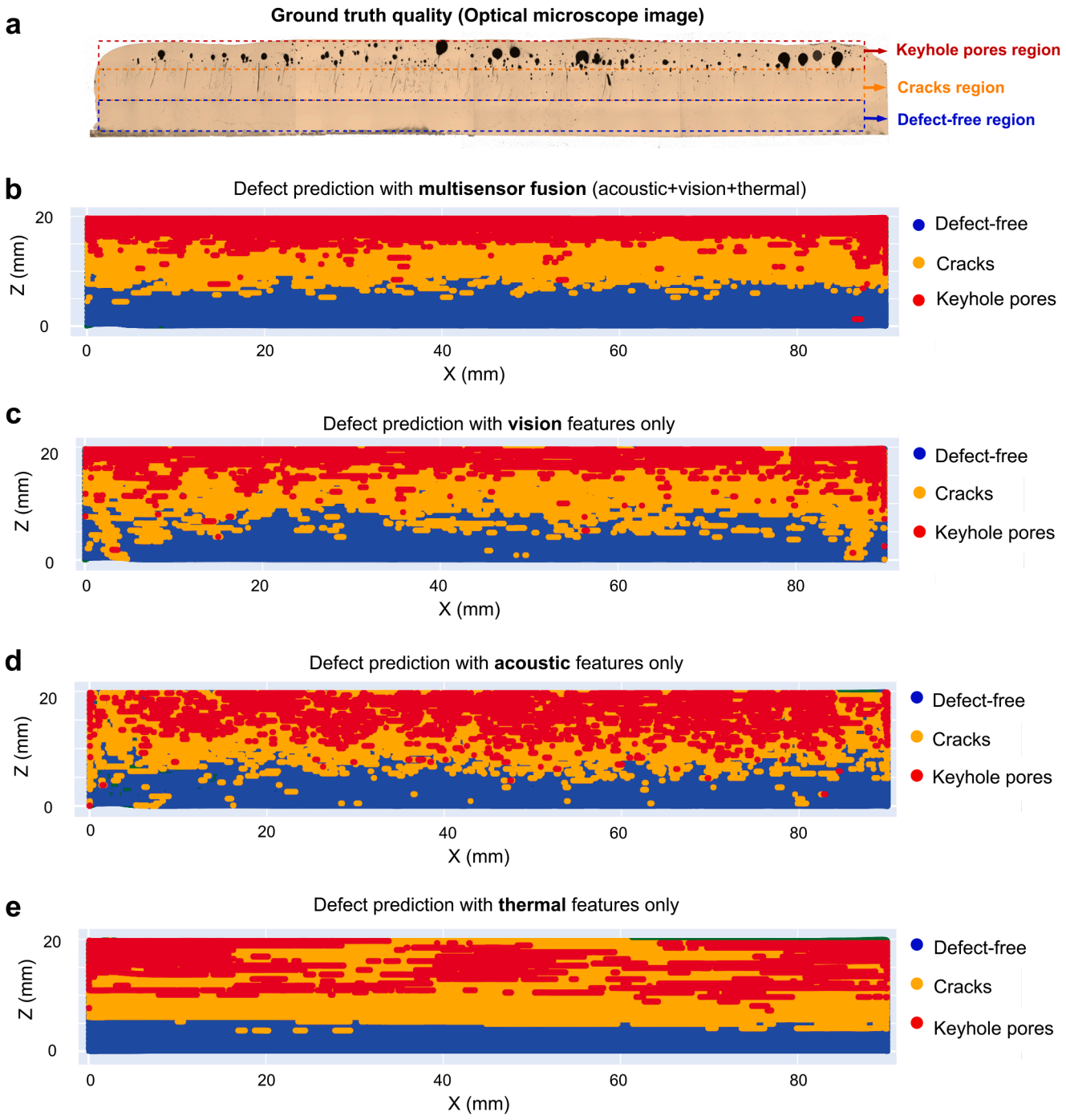


**Fig. 18.** Visualization and comparison of virtual quality map generated by the trained NN model: (a) ground truth defect obtained by optical microscope, showing defect-free regions in initial layers, cracks in in the middle layers, and keyhole pores in the upper layers. (b) defect prediction with multisensor fusion features, combining all acoustic, vision, and thermal features; (c) defect prediction with only vision features; (d) defect prediction with only acoustic features; (e) defect prediction with only thermal features.

occurrence is high, the laser power or robot speed can be adjusted to reduce localized heat accumulation.

iii As the proposed MFDT framework has been implemented in a dual-robot hybrid additive-subtractive manufacturing system (refer to Section 3.1), defective regions identified on the virtual quality map can be removed by robotic machining automatically at the locations predicted by the MFDT, before the subsequent layers are deposited.

We would like to highlight that establishing a reliable quality prediction model is the foundation for subsequent decision-making for physical process control. Future studies will focus on developing physical process control methods for adaptive quality enhancement based on the proposed MFDT.

## 5. Conclusions and future work

In this paper, a novel multisensor fusion-based digital twin (MFDT) framework was proposed for localized quality prediction in the robotic L-DED process. The main contribution of this study was to develop a spatiotemporal data fusion method for synchronizing and registering

multisensor features within the 3D volume of the printed part. A coaxial melt pool vision camera, an acoustic microphone sensor, and an off-axis infrared thermal camera were used to extract key features. Supervised machine learning models were trained on the multisensor fusion dataset to predict location-specific quality values such as defect-free, cracks, and keyhole pores. The predicted quality combined with location information was used to generate a virtual quality map that closely matched the physical quality of the printed component. Furthermore, the proposed MFDT performance surpassed the single-sensor-based defect prediction in terms of overall accuracy (96%), ROC-AUC score (99%), and false alarm rate (4.4%). Since the locations of defects were known within the dual-robot hybrid AM system's global coordinate frame, robotic machining can be employed to remove the defects and avoid further quality deterioration. As a result, the proposed MFDT provides a solid foundation for developing a self-adaptive hybrid processing strategy that is capable of improving part quality and removing defects automatically without human intervention.

One limitation of this work is that the use of thermal imaging is restricted to thin-walled parts. However, we believe that the proposed method can be extended to general bulk parts (i.e., multi-layer, multi-track) by adjusting the IR thermal camera's viewing angle. In a related study, Chen et al. [62] used off-axis thermal images to extract key thermal history features from L-DED-fabricated bulk samples for hardness distribution prediction. However, this approach may not work for more complex geometries where the thermal camera's field of view is blocked. One possible solution is to use multiple thermal cameras placed at different positions to capture the temperature distribution of the part from different viewpoints. This would overcome the limitation of only capturing the temperature from one side of the part. Another limitation of our current approach for localized defect registration is that it is limited to thin walls. However, we believe that the underlying physical phenomenon of keyhole pore formation and crack initiation is similar across different geometries (i.e., mainly due to localized heat accumulation). Therefore, the ML model trained using thin wall sample could also identify defects in other structures. To validate the effectiveness of our approach on 3D structures, we plan to conduct experiments on larger, more complex geometries in our future research. This will help to bridge the gap between this study and real-world defect detection applications. In addition, the proposed MFDT framework can potentially be used for process-structure-property (PSP) causal analytics in future studies. The input process parameter (e.g., laser power, scanning speed, powder feeding rate) combined with TCP position data (x, y, z coordinates) can be used to infer the quality and defects of as-printed parts [63], which could provide valuable information for process planning and closed-loop control. The proposed MFDT framework will also be extended to other materials and manufacturing processes, such as wire-arc additive manufacturing (WAAM) and wire-based L-DED.

## CRediT authorship contribution statement

**Lequn Chen:** Conceptualization, Methodology, Investigation, Formal analysis, Software, Data curation, Writing – original draft. **Guijun Bi:** Conceptualization, Writing – review & editing. **Xiling Yao:** Conceptualization, Methodology, Writing – review & editing, Funding acquisition. **Chaolin Tan:** Data curation, Writing – review & editing. **Jinlong Su:** Data curation, Investigation, Writing – review & editing. **Nicholas Poh Huat Ng:** Data curation, Writing – review & editing. **Youxiang Chew:** Project administration, Supervision, Writing – review & editing. **Kui Liu:** Supervision, Writing – review & editing. **Seung Ki Moon:** Writing – review & editing, Supervision, Project administration, Funding acquisition.

## Declaration of Competing Interest

The authors declare that they have no known competing financial interests or personal relationships that could have appeared to influence the work reported in this paper.

## Data availability

The data that has been used is confidential.

## Acknowledgments

This research is funded by the Agency for Science, Technology and Research (A*STAR) of Singapore through the Career Development Fund (Grant No. C210812030). It is also supported by Singapore Centre for 3D Printing (SC3DP), the National Research Foundation, Prime Minister's Office, Singapore under its Medium-Sized Centre funding scheme, as well as "The Belt and Road" Innovative Talent Exchange Foreign Experts Project (Grant No. DL2022030010L).

## References

[1] S.K. Moon, Y.E. Tan, J. Hwang, Y.-J. Yoon, Application of 3D printing technology for designing light-weight unmanned aerial vehicle wing structures, Int. J. of Precis. Eng. and Manuf.-Green Tech. 1 (3) (2014) 223–228, https://doi.org/10.1007/s40684-014-0028-x.

[2] R. Huang, et al., Energy and emissions saving potential of additive manufacturing: the case of lightweight aircraft components, Journal of Cleaner Production 135 (2016) 1559–1570, https://doi.org/10.1016/j.jclepro.2015.04.109.

[3] C. Tan, F. Weng, S. Sui, Y. Chew, G. Bi, Progress and perspectives in laser additive manufacturing of key aeroengine materials, International Journal of Machine Tools and Manufacture 170 (2021), 103804, https://doi.org/10.1016/j.ijmachtools.2021.103804.

[4] J.M. Wilson, C. Piya, Y.C. Shin, F. Zhao, K. Ramani, Remanufacturing of turbine blades by laser direct deposition with its energy and environmental impact analysis, Journal of Cleaner Production 80 (2014) 170–178, https://doi.org/10.1016/j.jclepro.2014.05.084.

[5] A. Gisario, M. Kazarian, F. Martina, M. Mehrpouya, Metal additive manufacturing in the commercial aviation industry: A review, Journal of Manufacturing Systems 53 (2019) 124–149, https://doi.org/10.1016/j.jmsy.2019.08.005.

[6] B. Blakey-Milner, et al., Metal additive manufacturing in aerospace: A review, Materials & Design 209 (2021), 110008, https://doi.org/10.1016/j.matdes.2021.110008.

[7] S.-H. Li, P. Kumar, S. Chandra, U. Ramamurty, Directed energy deposition of metals: processing, microstructures, and mechanical properties, International Materials Reviews 0 (0) (2022) 1–43, https://doi.org/10.1080/09506608.2022.2097411.

[8] Z. Li, et al., High deposition rate powder- and wire-based laser directed energy deposition of metallic materials: A review, International Journal of Machine Tools and Manufacture 181 (2022), 103942, https://doi.org/10.1016/j.ijmachtools.2022.103942.

[9] J.C. Haley, J.M. Schoenung, E.J. Lavernia, Observations of particle-melt pool impact events in directed energy deposition, Additive Manufacturing 22 (2018) 368–374, https://doi.org/10.1016/j.addma.2018.04.028.

[10] S.J. Wolff, et al., In situ X-ray imaging of pore formation mechanisms and dynamics in laser powder-blown directed energy deposition additive manufacturing, International Journal of Machine Tools and Manufacture 166 (2021), 103743, https://doi.org/10.1016/j.ijmachtools.2021.103743.

[11] H. Yeung, F.H. Kim, M.A. Donmez, J. Neira, Keyhole pores reduction in laser powder bed fusion additive manufacturing of nickel alloy 625, International Journal of Machine Tools and Manufacture 183 (2022), 103957, https://doi.org/10.1016/j.ijmachtools.2022.103957.

[12] Y. AbouelNour, N. Gupta, In-situ monitoring of sub-surface and internal defects in additive manufacturing: A review, Materials & Design 222 (2022), 111063, https://doi.org/10.1016/j.matdes.2022.111063.

[13] S. Guo, et al., Machine learning for metal additive manufacturing: Towards a physics-informed data-driven paradigm, Journal of Manufacturing Systems 62 (2022) 145–163, https://doi.org/10.1016/j.jmsy.2021.11.003.

[14] C. Xia, et al., A review on wire arc additive manufacturing: Monitoring, control and a framework of automated system, Journal of Manufacturing Systems 57 (2020) 31–45, https://doi.org/10.1016/j.jmsy.2020.08.008.

[15] F. He, et al., Research and application of artificial intelligence techniques for wire arc additive manufacturing: a state-of-the-art review, Robotics and Computer-Integrated Manufacturing 82 (2023), 102525, https://doi.org/10.1016/j.rcim.2023.102525.

[16] V. Azamfirei, F. Psarommatis, Y. Lagrosen, Application of automation for in-line quality inspection, a zero-defect manufacturing approach, Journal of Manufacturing Systems 67 (2023) 1–22, https://doi.org/10.1016/j.jmsy.2022.12.010.

[17] C. Liu, A.C.C. Law, D. Roberson, Z. (James) Kong, Image analysis-based closed loop quality control for additive manufacturing with fused filament fabrication, Journal of Manufacturing Systems 51 (2019) 75–86, https://doi.org/10.1016/j.jmsy.2019.04.002.

[18] Z. Snow, B. Diehl, E.W. Reutzel, A. Nassar, Toward in-situ flaw detection in laser powder bed fusion additive manufacturing through layerwise imagery and machine learning, Journal of Manufacturing Systems 59 (2021) 12–26, https://doi.org/10.1016/j.jmsy.2021.01.008.
[19] Q. Wang, W. Jiao, Y. Zhang, Deep learning-empowered digital twin for visualized weld joint growth monitoring and penetration control, Journal of Manufacturing Systems 57 (2020) 429–439, https://doi.org/10.1016/j.jmsy.2020.10.002.
[20] W. Li, et al., Deep learning based online metallic surface defect detection method for wire and arc additive manufacturing, Robotics and Computer-Integrated Manufacturing 80 (2023), 102470, https://doi.org/10.1016/j.rcim.2022.102470.
[21] H.-W. Cho, S.-J. Shin, G.-J. Seo, D.B. Kim, D.-H. Lee, Real-time anomaly detection using convolutional neural network in wire arc additive manufacturing: molybdenum material, Journal of Materials Processing Technology (2022), 117495, https://doi.org/10.1016/j.jmatprotec.2022.117495.
[22] L. Lu, J. Hou, S. Yuan, X. Yao, Y. Li, J. Zhu, Deep learning-assisted real-time defect detection and closed-loop adjustment for additive manufacturing of continuous fiber-reinforced polymer composites, Robotics and Computer-Integrated Manufacturing 79 (2023), 102431, https://doi.org/10.1016/j.rcim.2022.102431.
[23] J. Xiong, Y. Pi, H. Chen, Deposition height detection and feature point extraction in robotic GTA-based additive manufacturing using passive vision sensing, Robotics and Computer-Integrated Manufacturing 59 (2019) 326–334, https://doi.org/10.1016/j.rcim.2019.05.006.
[24] M. Akbari, R. Kovacevic, Closed loop control of melt pool width in robotized laser powder–directed energy deposition process, Int J Adv Manuf Technol 104 (5) (2019) 2887–2898, https://doi.org/10.1007/s00170-019-04195-y.
[25] L. Chen, X. Yao, Y. Chew, F. Weng, S.K. Moon, G. Bi, Data-Driven Adaptive Control for Laser-Based Additive Manufacturing with Automatic Controller Tuning, Applied Sciences 10 (22) (2020) 22, https://doi.org/10.3390/app10227967.
[26] F. Freeman, L. Chechik, B. Thomas, I. Todd, Calibrated closed-loop control to reduce the effect of geometry on mechanical behaviour in directed energy deposition, Journal of Materials Processing Technology 311 (2023), 117823, https://doi.org/10.1016/j.jmatprotec.2022.117823.
[27] X. Lin, Q. Wang, J.Y.H. Fuh, K. Zhu, Motion feature based melt pool monitoring for selective laser melting process, Journal of Materials Processing Technology 303 (2022), 117523, https://doi.org/10.1016/j.jmatprotec.2022.117523.
[28] L.E. Criales, Y.M. Arısoy, B. Lane, S. Moylan, A. Donmez, T. Özel, Laser powder bed fusion of nickel alloy 625: Experimental investigations of effects of process parameters on melt pool size and shape with spatter analysis, International Journal of Machine Tools and Manufacture 121 (2017) 22–36, https://doi.org/10.1016/j.ijmachtools.2017.03.004.
[29] M. Grasso, A.G. Demir, B. Previtali, B.M. Colosimo, In situ monitoring of selective laser melting of zinc powder via infrared imaging of the process plume, Robotics and Computer-Integrated Manufacturing 49 (2018) 229–239, https://doi.org/10.1016/j.rcim.2017.07.001.
[30] M. Khanzadeh, S. Chowdhury, M. Marufuzzaman, M.A. Tschopp, L. Bian, Porosity prediction: Supervised-learning of thermal history for direct laser deposition, Journal of Manufacturing Systems 47 (2018) 69–82, https://doi.org/10.1016/j.jmsy.2018.04.001.
[31] Y. Mao, et al., A deep learning framework for layer-wise porosity prediction in metal powder bed fusion using thermal signatures, J Intell Manuf (2022) 1–15, https://doi.org/10.1007/s10845-022-02039-3.
[32] D.A. Kriczky, J. Irwin, E.W. Reutzel, P. Michaleris, A.R. Nassar, J. Craig, 3D spatial reconstruction of thermal characteristics in directed energy deposition through optical thermal imaging, Journal of Materials Processing Technology 221 (2015) 172–186, https://doi.org/10.1016/j.jmatprotec.2015.02.021.
[33] S.M. Estalaki, C.S. Lough, R.G. Landers, E.C. Kinzel, T. Luo, Predicting defects in laser powder bed fusion using in-situ thermal imaging data and machine learning, Additive Manufacturing 58 (2022), 103008, https://doi.org/10.1016/j.addma.2022.103008.
[34] C.S. Lough, et al., Local prediction of Laser Powder Bed Fusion porosity by short-wave infrared imaging thermal feature porosity probability maps, Journal of Materials Processing Technology 302 (2022), 117473, https://doi.org/10.1016/j.jmatprotec.2021.117473.
[35] K. Gutknecht, M. Cloots, R. Sommerhuber, K. Wegener, Mutual comparison of acoustic, pyrometric and thermographic laser powder bed fusion monitoring, Materials & Design 210 (2021), 110036, https://doi.org/10.1016/j.matdes.2021.110036.
[36] S.A. Shevchik, C. Kenel, C. Leinenbach, K. Wasmer, Acoustic emission for in situ quality monitoring in additive manufacturing using spectral convolutional neural networks, Additive Manufacturing 21 (2018) 598–604, https://doi.org/10.1016/j.addma.2017.11.012.
[37] S.A. Shevchik, G. Masinelli, C. Kenel, C. Leinenbach, K. Wasmer, Deep Learning for In Situ and Real-Time Quality Monitoring in Additive Manufacturing Using Acoustic Emission, IEEE Transactions on Industrial Informatics 15 (9) (2019) 5194–5203, https://doi.org/10.1109/TII.2019.2910524.
[38] R. Drissi-Daoudi, et al., Differentiation of materials and laser powder bed fusion processing regimes from airborne acoustic emission combined with machine learning, Virtual and Physical Prototyping 0 (0) (2022) 1–24, https://doi.org/10.1080/17452759.2022.2028380.
[39] L. Chen, X. Yao, S.K. Moon, In-situ acoustic monitoring of direct energy deposition process with deep learning-assisted signal denoising, Materials Today: Proceedings (2022), https://doi.org/10.1016/j.matpr.2022.09.008.
[40] L. Chen, et al., In-situ crack and keyhole pore detection in laser directed energy deposition through acoustic signal and deep learning, Additive Manufacturing 69 (2023), 103547, https://doi.org/10.1016/j.addma.2023.103547.
[41] S.J. Altenburg, A. Straße, A. Gumenyuk, C. Maierhofer, In-situ monitoring of a laser metal deposition (LMD) process: comparison of MWIR, SWIR and high-speed NIR thermography, Quantitative InfraRed Thermography Journal 0 (0) (2020) 1–18, https://doi.org/10.1080/17686733.2020.1829889.
[42] L. Kong, X. Peng, Y. Chen, P. Wang, M. Xu, Multi-sensor measurement and data fusion technology for manufacturing process monitoring: a literature review, Int. J. Extrem. Manuf. 2 (2) (2020), 022001, https://doi.org/10.1088/2631-7990/ab7ae6.
[43] V. Pandiyan, et al., Deep learning-based monitoring of laser powder bed fusion process on variable time-scales using heterogeneous sensing and operando X-ray radiography guidance, Additive Manufacturing 58 (2022), 103007, https://doi.org/10.1016/j.addma.2022.103007.
[44] J. Li, X. Zhang, Q. Zhou, F.T.S. Chan, Z. Hu, A feature-level multi-sensor fusion approach for in-situ quality monitoring of selective laser melting, Journal of Manufacturing Processes 84 (2022) 913–926, https://doi.org/10.1016/j.jmapro.2022.10.050.
[45] J. Li, Q. Zhou, L. Cao, Y. Wang, J. Hu, A convolutional neural network-based multi-sensor fusion approach for in-situ quality monitoring of selective laser melting, Journal of Manufacturing Systems 64 (2022) 429–442, https://doi.org/10.1016/j.jmsy.2022.07.007.
[46] M. Perani, S. Baraldo, M. Decker, A. Vandone, A. Valente, B. Paoli, Track geometry prediction for Laser Metal Deposition based on on-line artificial vision and deep neural networks, Robotics and Computer-Integrated Manufacturing 79 (2023), 102445, https://doi.org/10.1016/j.rcim.2022.102445.
[47] J. Petrich, Z. Snow, D. Corbin, E.W. Reutzel, Multi-modal sensor fusion with machine learning for data-driven process monitoring for additive manufacturing, Additive Manufacturing 48 (2021), 102364, https://doi.org/10.1016/j.addma.2021.102364.
[48] P. Xu, X. Yao, L. Chen, K. Liu, G. Bi, Heuristic Kinematics of a Redundant Robot-Positioner System for Additive Manufacturing, in: 2020 6th International Conference on Control, Automation and Robotics (ICCAR), 2020, pp. 119–123, https://doi.org/10.1109/ICCAR49639.2020.9108047.
[49] L. Chen, X. Yao, N.P.H. Ng, S.K. Moon, In-situ Melt Pool Monitoring of Laser Aided Additive Manufacturing using Infrared Thermal Imaging, in: 2022 IEEE International Conference on Industrial Engineering and Engineering Management (IEEM), 2022, pp. 1478–1482, https://doi.org/10.1109/IEEM55944.2022.9989715.
[50] L. Chen, X. Yao, P. Xu, S.K. Moon, G. Bi, Surface Monitoring for Additive Manufacturing with in-situ Point Cloud Processing, in: 2020 6th International Conference on Control, Automation and Robotics (ICCAR), 2020, pp. 196–201, https://doi.org/10.1109/ICCAR49639.2020.9108092.
[51] P. Xu, et al., In-process adaptive dimension correction strategy for laser aided additive manufacturing using laser line scanning, Journal of Materials Processing Technology 303 (2022), 117544, https://doi.org/10.1016/j.jmatprotec.2022.117544.
[52] L. Chen, X. Yao, P. Xu, S.K. Moon, G. Bi, Rapid surface defect identification for additive manufacturing with in-situ point cloud processing and machine learning, Virtual and Physical Prototyping 16 (1) (2020) 50–67, https://doi.org/10.1080/17452759.2020.1832695.
[53] L. Chen, X. Yao, P. Xu, S.K. Moon, W. Zhou, G. Bi, In-Process Sensing, Monitoring and Adaptive Control for Intelligent Laser-Aided Additive Manufacturing, Transactions on Intelligent Welding Manufacturing (2023) 3–30, https://doi.org/10.1007/978-981-19-6149-6_1.
[54] A. García-Díaz, et al., OpenLMD, an open source middleware and toolkit for laser-based additive manufacturing of large metal parts, Robotics and Computer-Integrated Manufacturing 53 (2018) 153–161, https://doi.org/10.1016/j.rcim.2018.04.006.
[55] D. Faconti, "PlotJuggler 3.5." Jul. 17, 2022. Accessed: Jul. 17, 2022. [Online]. Available: https://github.com/facontidavide/PlotJuggler.
[56] B.T. Gibson, et al., Melt pool size control through multiple closed-loop modalities in laser-wire directed energy deposition of Ti-6Al-4V, Additive Manufacturing 32 (2020), 100993, https://doi.org/10.1016/j.addma.2019.100993.
[57] C. Knaak, J. von Eßen, M. Kröger, F. Schulze, P. Abels, A. Gillner, A Spatio-Temporal Ensemble Deep Learning Architecture for Real-Time Defect Detection during Laser Welding on Low Power Embedded Computing Boards, Sensors 21 (12) (2021) 12, https://doi.org/10.3390/s21124205.
[58] J. Jylänki, "An Exact Algorithm for Finding Minimum Oriented Bounding Boxes," 2015. https://www.semanticscholar.org/paper/An-Exact-Algorithm-for-Finding-Minimum-Oriented-Jyl%C3%A4nki/a76f7da5f8bae7b1fb4e85a65bd3812920c6d142 (accessed Jun. 30, 2022).
[59] "message_filters - ROS Wiki." http://wiki.ros.org/message_filters (accessed Jan. 16, 2023).
[60] J. Hauke, T. Kossowski, Comparison of Values of Pearson's and Spearman's Correlation Coefficients on the Same Sets of Data, Quaestiones Geographicae 30 (2) (2011) 87–93, https://doi.org/10.2478/v10117-011-0021-1.
[61] F. Pedregosa et al., "Scikit-learn: Machine Learning in Python," *MACHINE LEARNING IN PYTHON*, p. 6.
[62] Z. Chen, X. Guo, J. Shi, Hardness Prediction and Verification Based on Key Temperature Features During the Directed Energy Deposition Process, Int. J. of Precis. Eng. and Manuf.-Green Tech. (2020), https://doi.org/10.1007/s40684-020-00208-4.
[63] D. Knüttel, S. Baraldo, A. Valente, F. Bleicher, K. Wegener, E. Carpanzano, Machine learning based track height prediction for complex tool paths in direct metal deposition, CIRP Annals 71 (1) (2022) 193–196, https://doi.org/10.1016/j.cirp.2022.03.032.